The Astrophysical Journal, 988:157 (20pp), 2025 August 1 https://doi.org/10.3847/1538-4357/add727


# XMM-Newton Conclusively Identifies an Active Galactic Nucleus in a Green Pea Galaxy*

Peter G. Boorman[1,2], Jiří Svoboda[2], Daniel Stern[3], Bret D. Lehmer[4,5], Abhijeet Borkar[2], Murray Brightman[1], Hannah P. Earnshaw[1], Fiona A. Harrison[1], Konstantinos Kouroumpatzakis[2], Barbora Adamcová[2], Roberto J. Assef[6], Matthias Ehle[7], Brian Grefenstette[1], Romana Grossová[2,8], Maitrayee Gupta[2], Elias Kammoun[1], Taiki Kawamuro[9], Lea Marcotulli[10,11,1], Romana Mikušincová[12], Matthew J. Middleton[13], Edward Nathan[1], Joanna M. Piotrowska[1], Jean J. Somalwar[1], Núria Torres-Albà[14,17], Dominic J. Walton[15], and Daniel R. Weisz[16]
[1] Cahill Center for Astrophysics, California Institute of Technology, 1216 East California Boulevard, Pasadena, CA 91125, USA; boorman@caltech.edu
[2] Astronomical Institute, Academy of Sciences, Boční II 1401, CZ-14131 Prague, Czech Republic
[3] Jet Propulsion Laboratory, California Institute of Technology, Pasadena, CA 91109, USA
[4] Department of Physics, University of Arkansas, 226 Physics Building, 825 West Dickson Street, Fayetteville, AR 72701, USA
[5] Arkansas Center for Space and Planetary Sciences, University of Arkansas, 332 N. Arkansas Avenue, Fayetteville, AR 72701, USA
[6] Instituto de Estudios Astrofísicos, Facultad de Ingeniería y Ciencias, Universidad Diego Portales, Av. Ejército Libertador 441, Santiago, Chile
[7] European Space Agency, European Space Astronomy Centre (ESA/ESAC), Camino Bajo del Castillo s/n, 28692 Villanueva de la Cañada, Madrid, Spain
[8] Department of Theoretical Physics and Astrophysics, Faculty of Science, Masaryk University, Kotlářská 2, Brno 61137, Czech Republic
[9] Department of Earth and Space Science, Osaka University, 1-1 Machikaneyama, Toyonaka 560-0043, Osaka, Japan
[10] Yale Center for Astronomy & Astrophysics, 52 Hillhouse Avenue, New Haven, CT 06511, USA
[11] Department of Physics, Yale University, P.O. Box 208120, New Haven, CT 06520, USA
[12] INAF Istituto di Astrofisica e Planetologia Spaziali, Via del Fosso del Cavaliere 100, I-00133 Roma, Italy
[13] Department of Physics & Astronomy, Faculty of Physical Sciences and Engineering, University of Southampton, Southampton, SO17 1BJ, UK
[14] Department of Astronomy, University of Virginia, P.O. Box 400325, Charlottesville, VA 22904, USA
[15] Centre for Astrophysics Research, University of Hertfordshire, College Lane, Hatfield AL10 9AB, UK
[16] Department of Astronomy, University of California, Berkeley, CA 94720, USA
*Received 2025 February 25; revised 2025 May 5; accepted 2025 May 10; published 2025 July 21*

## Abstract

Green Pea galaxies are a class of compact, low-mass, low-metallicity star-forming galaxies in the relatively local Universe. They are believed to be analogs of high-redshift galaxies that reionized the Universe, and, indeed, the James Webb Space Telescope (JWST) is now uncovering such populations at record redshifts. Intriguingly, JWST finds evidence suggestive of active galactic nuclei (AGN) in many of these distant galaxies, including the elusive Little Red Dots, which broadly lack any detectable X-ray counterparts. Intuitively, one would expect to detect an AGN in their low-redshift analogs with X-rays, yet no study to date has conclusively identified an X-ray AGN within a Green Pea galaxy. Here we present the deepest X-ray campaign of a Green Pea galaxy performed to date, obtained with the goal of discerning the presence of a (potentially low-luminosity) AGN. The target—SDSS J082247.66+224144.0 (hereafter J0822+2241)—was previously found to display a comparable X-ray spectral shape to more local AGN ($\Gamma \sim 2$) and a high luminosity ($L_{2-10\,\mathrm{keV}} \sim 10^{42}\,\mathrm{erg\,s^{-1}}$). We show that over 6.2 yr (rest frame) the 2–10 keV luminosity of J0822+2241 is constant, whereas the soft 0.5–2 keV flux has decreased significantly by ∼60%. We discuss possible scenarios to explain the X-ray properties of J0822+2241, finding transient low column density obscuration surrounding an AGN to be the only plausible scenario. J0822+2241 thus provides further evidence that low-luminosity AGN activity could have contributed to the epoch of reionization and that local analogs are useful to derive a complete multiwavelength picture of black hole growth in high-redshift, low-luminosity AGNs.

*Unified Astronomy Thesaurus concepts:* Starburst galaxies (1570); Active galaxies (17); Compact galaxies (285); X-ray active galactic nuclei (2035)

## 1. Introduction

Early cosmic epochs (i.e., $z \gtrsim 6$) were a crucial time in the history of the Universe, corresponding to the period when energetic photons ionized and heated the intergalactic medium, leading to the end of the cosmic dark ages (e.g., R. J. Bouwens et al. 2015; B. E. Robertson et al. 2015). The source of such ionizing photons is still a matter of debate. Neutral hydrogen readily absorbs and is ionized by ultraviolet photons. Thus, the two most prominent sources of astrophysical ultraviolet flux—accretion onto massive black holes and young populations of massive stars within compact low-mass galaxies—are two prime candidates to have powered the epoch of reionization (e.g., P. R. Shapiro & M. L. Giroux 1987; A. Loeb & R. Barkana 2001; N. Torres-Albà et al. 2020). X-ray photons could have also contributed to reionization, with accretion onto massive black holes and X-ray binary populations being the two most likely astrophysical contenders (T. Fragos et al. 2013). Though at ultraviolet and X-ray wavelengths many studies previously suggested that quasars should have been too rare at $z \gtrsim 6$ to dominate cosmic reionization (e.g., F. Fontanot

* Based on observations obtained with XMM-Newton, an ESA science mission with instruments and contributions directly funded by ESA Member States and NASA.
[17] GECO Fellow.

et al. 2012; T. Fragos et al. 2013; F. Haardt & R. Salvaterra 2015), numerous candidate active galactic nuclei (AGN) unveiled by the James Webb Space Telescope (JWST; J. P. Gardner et al. 2023) have suggested that accretion onto massive black holes in AGN with lower luminosities than powerful quasars may be a viable possibility after all (e.g., R. P. Naidu et al. 2022; Y. Harikane et al. 2023; D. D. Kocevski et al. 2023; G. Yang et al. 2023; S. Asthana et al. 2024; J. E. Greene et al. 2024; P. Madau et al. 2024; H. Übler et al. 2024).

JWST has led to the discovery of many $z > 6$ galaxies (including the so-called Little Red Dots; J. Matthee et al. 2023) with broad permitted optical lines consistent with low-luminosity AGN. However, the lack of X-ray detections for the bulk of the population has led to ambiguity between extreme star formation processes and AGN (e.g., T. T. Ananna et al. 2024; M. Yue et al. 2024; R. Maiolino et al. 2025). At lower redshifts, X-ray observations provide one of the most efficient methods for both selecting and characterizing AGN (e.g., W. N. Brandt & D. M. Alexander 2015; R. C. Hickox & D. M. Alexander 2018). In particular, detailed X-ray spectral analyses have proven powerful in understanding the obscuration properties of AGN, including low-luminosity AGN (e.g., J. Aird et al. 2015; J. Buchner et al. 2015; C. Ricci et al. 2015; A. Annuar et al. 2020; P. G. Boorman et al. 2024b, 2024a, 2025; F. Civano et al. 2024). A unique perspective on the role of AGN versus star formation processes to cosmic reionization is therefore attainable from nearby analogs of high-redshift galaxies for which more detailed X-ray studies can be performed (e.g., T. Kawamuro et al. 2019; J. Svoboda et al. 2019; B. Adamcová et al. 2024; A. Borkar et al. 2024; K. Kouroumpatzakis et al. 2024; M. Singha et al. 2025).

Green Pea galaxies represent such a class of objects. First discovered by C. Cardamone et al. (2009) from the Sloan Digital Sky Survey (SDSS; D. G. York et al. 2000), Green Pea galaxies are now known to be compact (half-light radii $\lesssim 5$ kpc), low-mass ($M_* \lesssim 3 \times 10^9\,M_\odot$), low-metallicity ($\log[\mathrm{O/H}] + 12 \sim 8.1$) star-forming galaxies with high star formation rates ($\gtrsim 10\,M_\odot\,\mathrm{yr}^{-1}$). Green Pea galaxies are also one of the closest (typically with $z \lesssim 0.3$) galaxies known to exhibit significant Lyman continuum leakage to a level that is compatible with models of cosmic reionization (Y. I. Izotov et al. 2016). Most recently, Green Pea galaxies displaying broad permitted lines have shown to be local analogs of JWST-detected Little Red Dots owing to their strikingly similar V-shaped rest-frame UV-to-optical spectra, compact morphologies, and broad permitted lines akin to narrow-line Seyfert 1 galaxies or regular broad-line Seyfert 1 galaxies (R. Lin et al. 2025).

However, detailed X-ray spectroscopic studies of Green Pea galaxies to infer the presence of an AGN have proven scarce to date. The pioneering work of J. Svoboda et al. (2019) revealed some unexpected X-ray properties for a sample of three Green Peas identified from the original C. Cardamone et al. (2009) sample. Two of the three galaxies were found to be overluminous by a factor of approximately five relative to empirical scaling relations that predict the level of X-ray luminosity expected as a function of metallicity and star formation (e.g., B. D. Lehmer et al. 2010; M. Brorby et al. 2016). This paper presents a detailed analysis of one Green Pea galaxy from the sample of J. Svoboda et al. (2019), SDSS J082247.66+224144.0 (hereafter J0822+2241). At a redshift of $z = 0.216$, detailed Hubble Space Telescope/Cosmic Origins Spectrograph near-UV (NUV) observations confirmed a compact galaxy with a half-light radius of 680 pc (H. Yang et al. 2017). The star formation rate, stellar mass, and metallicity have additionally been estimated to be $37 \pm 4\,M_\odot\,\mathrm{yr}^{-1}$, $M_* = 3 \times 10^8\,M_\odot$, and $\log(\mathrm{O/H}) + 12 = 8.1$, respectively (G. Kauffmann et al. 2003; J. Brinchmann et al. 2004; C. Cardamone et al. 2009; Y. I. Izotov et al. 2011; J. Svoboda et al. 2019). However, the previous analyses of the SDSS optical spectrum considered that there was a general lack of any detectable AGN component. Narrow-line ratios plotted on the H$\alpha$/[N II] versus H$\beta$/[O III] Baldwin, Phillips, and Terlevich diagram (J. A. Baldwin et al. 1981) were consistent with theoretical expectations from star formation (J. Svoboda et al. 2019), and no common optical coronal emission lines indicative of massive black hole activity were significantly detected (M. Reefe et al. 2023).

However, in X-rays J0822+2241 displayed a broadband X-ray continuum redolent of local AGN with an observed photon index $2.0 \pm 0.4$ in the 0.3–10 keV passband. The rest-frame 0.5–8 keV X-ray luminosity of the source was additionally found to be substantial at $L_{0.5-8\,\mathrm{keV}} = 1.2^{+0.2}_{-0.3} \times 10^{42}\,\mathrm{erg\,s^{-1}}$, compatible with the X-ray luminosities of local Seyfert AGN (e.g., C. Ricci et al. 2017a; A. Annuar et al. 2020). T. Kawamuro et al. (2019) showed that the near-to-mid-infrared color of J0822+2241 measured by the Wide-field Infrared Survey Explorer (WISE) was remarkably similar to the red colors found by powerful quasars and mid-infrared-dominated AGN in the more local Universe (e.g., T. H. Jarrett et al. 2011; S. Mateos et al. 2012; D. Stern et al. 2012; R. J. Assef et al. 2018; S. Satyapal et al. 2018; D. Asmus et al. 2020). However, as pointed out by K. N. Hainline et al. (2016; see also M. R. Sturm et al. 2025), the near-to-mid-infrared colors expected from extreme star formation in compact galaxies with correspondingly high specific star formation rates can be arbitrarily red, in close similarity to the red colors expected from dominant AGN. Indeed, T. Kawamuro et al. (2019) proved with extensive simulations that combined the same XMM-Newton data analyzed by J. Svoboda et al. (2019) with nondetections at $> 10$ keV from snapshot observations with the Nuclear Spectroscopic Telescope ARray (NuSTAR; F. A. Harrison et al. 2013) either that J0822+2241 is a Compton-thick type 2 quasar observed in scattered light with a relatively unobscured spectral shape at $<10$ keV or that the near-to-mid-infrared colors of the source cannot be reliably used as a bolometric indicator of AGN power. Additional insights were provided by A. Franeck et al. (2022), who showed that hot gas could not explain the high X-ray luminosity of the source. B. Adamcová et al. (2024) then calculated the expected X-ray emission from X-ray binaries in J0822+2241 by integrating a gas-phase metallicity-dependent X-ray luminosity function from B. D. Lehmer et al. (2021). By self-consistently accounting for star formation rate, metallicity, and stochasticity effects, the authors showed that the observed 0.5–8 keV luminosity of J0822+2241 could not have a contribution from X-ray binaries greater than ∼20%. J0822+2241 thus represents one of the strongest Green Pea X-ray AGN candidates identified to date. However, a substantial 2–10 keV luminosity and observed spectral index from a single relatively short exposure were insufficient to conclusively decipher its AGN nature.

**Table 1**
XMM-Newton Data Used in This Work

| Obs. ID | Label | Obs. Start (UT) | $\mathcal{T}$ (ks) | $\mathcal{C}_{\rm broad}$ (counts ks$^{-1}$) | $\mathcal{C}_{\rm broad}$ (counts ks$^{-1}$) | $\mathcal{C}_{\rm broad}$ (counts ks$^{-1}$) | $\mathcal{S}_{\rm broad}$ | $\mathcal{S}_{\rm broad}$ | $\mathcal{S}_{\rm broad}$ |
|---|---|---|---|---|---|---|---|---|---|
| (1) | (2) | (3) | (4) | (5) | (6) | (7) | (8) | (9) | (10) |
| 0690470201 | Epoch 1 | 2013 Apr 6, 04:46 | 28.3 | $2.47 \pm 0.43$ | $0.74 \pm 0.40$ | $3.21 \pm 0.59$ | 5.9 | 1.8 | 5.5 |
| 0865450301 | Epoch 2a | 2020 Oct 13, 12:46 | 68.7 | $1.13 \pm 0.27$ | $1.06 \pm 0.25$ | $2.19 \pm 0.37$ | 4.2 | 4.3 | 6.0 |
| 0865450401 | Epoch 2b | 2020 Nov 10, 10:08 | 42.0 | $1.16 \pm 0.36$ | $0.69 \pm 0.36$ | $1.87 \pm 0.51$ | 3.2 | 1.9 | 3.7 |
| … | Epoch 2 (2a + 2b) | … | 110.7 | $1.14 \pm 0.17$ | $0.92 \pm 0.16$ | $2.07 \pm 0.23$ | 5.3 | 4.4 | 6.9 |

**Note.** Column (1): observation ID. Column (2): observation label used in this work. Column (3): observation start date and time. Column (4): net exposure time in ks. Columns (5)–(7): net count rate in counts ks$^{-1}$ for the soft (0.3–2 keV), hard (2–10 keV), and broad (0.3–10 keV) bands, respectively. Columns (8)–(10): signal-to-noise ratio in the soft, hard, and broad bands, respectively, computed with the `gv_significance` library of G. Vianello (2018). See https://github.com/giacomov/gv_significance.

Here we present a detailed X-ray spectral and broadband investigation into J0822+2241 using 111 ks of new data from two observations with the XMM-Newton observatory (PI: P. Boorman). Combined with the archival 28 ks of XMM-Newton data (PI: M. Ehle), this study represents the deepest X-ray observation of a Green Pea galaxy performed to date. In Section 2 we present the X-ray observations of J0822+2241 together with a description of the X-ray, optical, and broadband spectral methodology we use in this work. Section 3 then presents the results of our multiepoch X-ray spectral analysis of J0822+2241, followed by a discussion of the viable scenarios for the physical origin of its X-ray properties in Section 5. Section 6 then compares the properties of J0822+2241 to a comparable sample of JWST-detected AGN, before a brief summary of our findings is given in Section 7.

## 2. Data and Method

Details of all three XMM-Newton (F. Jansen et al. 2001) observations used in this work are given in Table 1. All data were analyzed with the Scientific Analysis System (SAS; C. Gabriel et al. 2004) v.20.0.0. The EPIC-pn (L. Strüder et al. 2001) observation data files were processed using the SAS command EPPROC to generate calibrated and concatenated events files. Intervals of background flaring activity were filtered using light curves generated in energy ranges recommended in the SAS threads.[18] Corresponding images for the pn detector were generated using the command EVSELECT, and source spectra were extracted from circular regions centered on the SDSS coordinates of J0822+2241 after accounting for any astrometric offsets by eye. Background regions of similar size to the source regions were defined following the XMM-Newton Calibration Technical Note XMM-SOC-CAL-TN-0018 (M. J. S. Smith 2025), ensuring that the distance from the readout node was similar to that of the source region. The EPIC-pn source and background spectra were then extracted with EVSELECT with patterns less than four. Finally, response and ancillary response matrices were created with the RMFGEN and ARFGEN tools. Each of the three EPIC-pn observations were performed with the Thin Filter in Full Frame mode. We do not use EPIC-MOS (M. J. L. Turner et al. 2001) data in this work since the improvement in sensitivity in combination with EPIC-pn was not substantial and contributed to an increase in computation time associated with simultaneously fitting all spectra together.

Both epochs 2a and 2b in Table 1 have consistent soft, hard, and broad passband count rates. Thus, we coadded the spectra using the `ftooladdspec`.[19] All XMM-Newton analysis presented hereafter thus refers to epoch 1 as the observation in 2013 and epoch 2 as the spectrum derived from coadding the two observations in 2020.

All X-ray spectral fitting presented in this paper was performed with PyXspec (K. A. Arnaud 1996; C. Gordon & K. Arnaud 2021) using the modified $C$-statistic[20] (W. Cash 1979; K. Wachter et al. 1979). All parameter exploration was carried out with the Bayesian X-ray Analysis software package (BXA v4.0.5; J. Buchner et al. 2014; J. Buchner 2016), using the nested sampling package UltraNest v4.0.5 (J. Buchner 2021). All parameters were assigned uniform or log-uniform priors depending on their nature (i.e., whether it ranges over many orders of magnitude), unless stated otherwise. All spectral fits used a source redshift of $z = 0.216$ and included Galactic absorption along the line of sight with column density $N_{\rm H} = 4.75 \times 10^{20}$ cm$^{-2}$ (R. Willingale et al. 2013) using the `TBabs` model and abundances from J. Wilms et al. (2000).

We rely on quantile–quantile plots for goodness-of-fit verification of the X-ray spectral fits in this work. Fundamentally quantile–quantile plots encompass the same information as more conventional residuals, in that the detected (source + background) counts are compared to the model-predicted counts as a means to understand whether a given model can explain the data in an acceptable manner. However, for quantile–quantile plots, the detected and model-predicted counts are summed across the unbinned detector channels cumulatively (depicted as $\mathcal{Q}_{\rm data}$ and $\mathcal{Q}_{\rm model}$, respectively, throughout this work). For interpretative convenience, rather than relying on a plot presenting $\mathcal{Q}_{\rm data}$ versus $\mathcal{Q}_{\rm model}$, we instead plot detected energy versus $\mathcal{Q}_{\rm data} - \mathcal{Q}_{\rm model}$, more akin to conventional energy versus data – model residuals (sometimes referred to as quantile–quantile difference plots; J. Buchner & P. Boorman 2023; P. G. Boorman et al. 2024a). There are important distinctions to consider in comparison to standard data – model residuals, though. For example, a peak or trough present in energy versus $\mathcal{Q}_{\rm data} - \mathcal{Q}_{\rm model}$ informs us that the largest data excess relative to the model or the largest model excess relative to the data occurs below the energy of that peak or trough, respectively. There are also a number of advantages to performing model verification in terms of quantiles rather

[18] For more information, see https://www.cosmos.esa.int/web/xmm-newton/sas-thread-epic-filterbackground.

[19] https://heasarc.gsfc.nasa.gov/ftools/caldb/help/addspec.txt

[20] https://heasarc.gsfc.nasa.gov/xanadu/xspec/manual/XSappendixStatistics.html

than standard residuals. First, quantile–quantile plots sum counts on the intrinsic detector energy resolution and do not require binning. Therefore, in the event of low signal-to-noise ratio data, valuable inference can still be acquired without requiring any loss of information. Second, by simulating a given model fit with the instrumental setup of the detector (i.e., the same background, response, and exposure time), one can plot the predicted range in $\mathcal{Q}_{\rm data}-\mathcal{Q}_{\rm model}$ expected from the imperfect nature of the detector in the event that the model was correct. The corresponding posterior-predictive range can therefore be used to quantify when fluctuations in $\mathcal{Q}_{\rm data}-\mathcal{Q}_{\rm model}$ are statistically significant. All quantile–quantile difference plots in this work provide the 90% posterior-predictive range as dark-gray shaded regions. We consider any deviation in $\mathcal{Q}_{\rm data}-\mathcal{Q}_{\rm model}$ that is significantly outside a given posterior-predictive range to be significant to $\geqslant$90% confidence.

To complement our X-ray spectral fitting, we reanalyze the archival SDSS spectrum of J0822+2241 (SDSS `SpecObjID` 2168502517682432000) to primarily search for a broad component to the H$\alpha$ line. We find a signal-to-noise ratio of $\gtrsim$70 and $\sim$5–7 in H$\alpha$ and the continuum over the 6400–6700 Å passband, respectively. To analyze the spectrum, we use BXA v2.10 with the nested sampling package `PyMultiNest` (F. Feroz et al. 2009; J. Buchner et al. 2014) within `PyXspec`. To load the spectrum into `Xspec`, we use the HEASoft tool `ftflx2xsp` to convert the SDSS spectrum into an `Xspec`-readable format. All line luminosities reported from the optical spectral fitting have been corrected for Milky Way extinction using the nebular color excess estimation from E. F. Schlafly & D. P. Finkbeiner (2011)[21] and the extinction law of E. L. Fitzpatrick (1999) via the `extinction` Python package.[22] The total estimated reddening arising along the line of sight to J0822+2241 from the Milky Way is $E(B-V)=0.039$ mag, amounting to a multiplicative flux correction factor of 1.06 and 1.11 at the observed-frame wavelengths of H$\alpha$ and H$\beta$, respectively.

To obtain independent estimates of the galaxy and AGN properties, we performed broadband spectral energy distribution (SED) fitting across the X-ray–infrared wavelength regime using the `Lightning` package (K. Doore et al. 2023; B. D. Lehmer et al. 2024).[23] Following the procedures outlined in Section 3 of B. D. Lehmer et al. (2024), we culled imaging data available in the archives from various facilities, including Galaxy Evolution Explorer (GALEX), Swift/UVOT, SDSS, Pan-STARRS, and WISE,[24] and convolved all data to a common 20″ full width at half-maximum (FWHM) point-spread function. Photometry was subsequently extracted from all bands using a circular aperture with a 33″ radius. We expanded our SED to include the XMM-Newton count spectrum for epoch 2 in four additional X-ray bandpasses. In total, our broadband SED includes 19 photometric measurements spanning the X-ray to mid-infrared. When fitting the SED with `Lightning`, we followed the methods detailed in E. B. Monson et al. (2023), assuming that both stellar populations and AGN are able to contribute. In this framework, the AGN is modeled using `qsosed` (A. Kubota & C. Done 2018) to account for the intrinsic accretion disk spectral shape and `SKIRTOR` (M. Stalevski et al. 2012, 2016) to model inclination-dependent dust obscuration and emission from a dusty torus. Included among the full set of parameters (see Table 4 of E. B. Monson et al. 2023) is the star formation history in five discrete age bins, which enables the derivation of star formation rate, galaxy stellar mass, and the central black hole mass of the AGN.

All spectral parameters throughout the paper are quoted as the maximum a posteriori value together with the 90% highest density interval integrated from the marginalized posterior mode, unless stated otherwise. We additionally use $u$ to describe unconstrained parameter bounds. Luminosities are calculated assuming the cosmological parameters $H_0=70\,{\rm km\,s^{-1}\,Mpc^{-1}}$, $\Omega_m=0.3$, $\Omega_\Lambda=0.7$, which correspond to a luminosity distance to J0822+2241 at $z=0.216$ of 1.07 Gpc.

## 3. Results

### 3.1. X-Ray Spectral Analysis

First, we focus on a phenomenological X-ray spectral parameterization of J0822+2241 in both XMM-Newton epochs separately. The upper portion of Table 2 and Figure 1 shows the spectral fits with a redshifted power law to epochs 1 and 2. For epoch 1, we find an observed photon index of $1.7^{+0.5}_{-0.6}$, consistent with the value of $2.0\pm0.4$ derived by J. Svoboda et al. (2019). Additionally in agreement with J. Svoboda et al. (2019), we find a substantial rest-frame absorption-uncorrected 2–10 keV luminosity of $\log L_{2-10\,{\rm keV}}/{\rm erg\,s^{-1}}=42.0\pm0.3$ for J0822+2241 in epoch 1. The second epoch of data, taken $\sim$6.2 yr later in the rest frame of J0822+2241, provides a means to search for X-ray variability in the target. We find that the hard 2–10 keV X-ray rest-frame absorption-uncorrected luminosity of J0822+2241 is fully consistent with being constant between both epochs. However, the 0.5–2 keV luminosities and associated uncertainties suggest a decrease of $\sim$0.3 dex between epochs 1 and 2. The corresponding decrease in soft flux also results in a very hard observed photon index in epoch 2 of $\Gamma=0.8^{+0.2}_{-0.3}$, significantly outside the typical distribution of intrinsic (i.e., absorption-corrected) photon indices found for local AGN samples, which tends to peak at $\sim$1.6–1.9 (e.g., K. Nandra & K. A. Pounds 1994; C. Ricci et al. 2017a).

To understand whether the apparent spectral change between either epoch is significant, we check whether the posterior model derived for epoch 1 can explain the data from epoch 2 satisfactorily and vice versa. Figure 2 presents the same folded X-ray spectral data as in Figure 1, except that the posterior models from either epoch have been switched. From the top panels alone, it is clear that either model cannot explain the observed data $\lesssim$2 keV from the opposite epoch. In the bottom panels, we show the quantile–quantile difference curves as a means to quantify the significance of the X-ray spectral shape change $\lesssim$2 keV. Since the gray shaded posterior-predictive regions in either bottom panel rely on the same data as in Figure 1, the resulting gray shaded regions are very similar to Figure 1 as well. For the bottom left panel of Figure 2, the $\mathcal{Q}_{\rm data}-\mathcal{Q}_{\rm model}$ curve presents a peak at $\sim$2 keV significantly offset from the 90% shaded posterior-predictive region. Since the

[21] Acquired via the NASA/IPAC Galactic Dust Reddening and Extinction tool; https://irsa.ipac.caltech.edu/applications/DUST/.

[22] https://extinction.readthedocs.io/en/latest/

[23] https://github.com/ebmonson/lightningpy

[24] GALEX and Swift/UVOT data were obtained from the Mikulski Archive for Space Telescopes (MAST; https://mast.stsci.edu/); SDSS, from DR18 via SkyServer (https://skyserver.sdss.org/); Pan-STARRS, from the PS1 Image Access portal (https://ps1images.stsci.edu/cgi-bin/ps1cutouts); and WISE, from the NASA/IPAC Infrared Science Archive (IRSA; https://irsa.ipac.caltech.edu/).

**Table 2**
X-Ray Spectral Parameters Constrained in This Work

| Parameter | Passband (keV) | Epoch 1 | Epoch 2 | Units |
|---|---|---|---|---|
| (1) | (2) | (3) | (4) | (5) |
| Phenomenological Model Parameters (see Section 3.1) model = TBabs × zpowerlw | | | | |
| $\Gamma$ | … | $1.7^{+0.5}_{-0.6}$ | $0.8^{+0.2}_{-0.3}$ | … |
| log $F_{\rm obs}$[a] | 0.5–2 | $-14.4 \pm 0.1$ | $-14.7 \pm 0.1$ | erg s$^{-1}$ cm$^{-2}$ |
| log $F_{\rm obs}$[a] | 2–10 | $-14.0^{+0.3}_{-0.4}$ | $-13.8 \pm 0.1$ | erg s$^{-1}$ cm$^{-2}$ |
| log $L_{\rm obs}$[b] | 0.5–2 | $41.7 \pm 0.1$ | $41.4 \pm 0.1$ | erg s$^{-1}$ |
| log $L_{\rm obs}$[b] | 2–10 | $42.0 \pm 0.3$ | $42.2 \pm 0.1$ | erg s$^{-1}$ |
| Obscured AGN Physical Model Parameters (see Section 5.1) model = TBabs × zTBabs × cabs × zpowerlw | | | | |
| log $n_{\rm h}$ | … | $20.7^{+0.7}_{-u}$ | $21.8 \pm 0.3$ | cm$^{-2}$ |
| log($N_{\rm H,2}/N_{\rm H,1}$)[c] | … | $1.08^{+0.66}_{-0.72}$ | | … |
| $\Gamma$ | … | $1.7^{+0.1}_{-0.2}$ | | … |
| log($L_{\rm 1,obs}/L_{\rm 2,obs}$)[d] | 0.5–2 | $0.22^{+0.13}_{-0.12}$ | | … |
| log($L_{\rm 1,obs}/L_{\rm 2,obs}$)[d] | 2–10 | $0.01 \pm 0.01$ | | … |
| log $L_{\rm int}$[e] | 0.5–2 | $41.8 \pm 0.1$ | | erg s$^{-1}$ |
| log $L_{\rm int}$[e] | 2–10 | $42.1 \pm 0.1$ | | erg s$^{-1}$ |

**Notes.** Column (1): parameter of interest. Column (2): passband that a corresponding parameter was measured over. Columns (3) and (4): observed parameter value measured for the epoch 1 and 2 X-ray spectra, respectively. Column (5): units of the parameter of interest.
[a] Absorption-uncorrected observed-frame flux.
[b] Absorption-uncorrected rest-frame luminosity.
[c] Logarithmic column density ratio between epochs 2 and 1.
[d] Logarithmic absorption-uncorrected rest-frame luminosity ratio between epochs 1 and 2.
[e] Absorption-corrected rest-frame luminosity.

curve is cumulative, we can infer that the largest epoch 1 data excess relative to the epoch 2 posterior model is $\lesssim$2 keV and significant to >90% confidence. The opposite is true in the bottom right panel of Figure 2, in which the epoch 2 data are suppressed relative to the epoch 1 model posterior to >90% confidence. We note that in generating the $\mathcal{Q}_{\rm data} - \mathcal{Q}_{\rm model}$ curves and posterior-predictive ranges we deliberately simulate multiple posterior rows multiple times rather than a single best fit in order to encompass the full possible posterior spectral range allowed by either fit. To our knowledge, this is the first statistically significant detection of X-ray spectral variability from a Green Pea galaxy. However, these X-ray spectral tests are purely phenomenological and do not necessarily provide a causal link between each epoch. We defer the reader to Section 5.1 for a physically plausible cause of this flux change.

### 3.2. Optical Spectral Analysis

Complimentary to our X-ray analysis, we additionally search for signatures of an AGN in J0822+2241 via spectral fitting of the archival SDSS spectrum. Our fitting procedure was primarily constructed to follow that of A. E. Reines et al. (2013), in which a fitting procedure was devised to search for faint yet statistically significant evidence of broad components to H$\alpha$. To account for the underlying continuum produced from different stellar populations, we first used the penalized PiXel Fitting software (pPXF; M. Cappellari & E. Emsellem 2004), which includes emission from host galaxy starlight including Balmer absorption lines. However, there were no strongly detectable absorption features in the observed SDSS passband for pPXF to constrain stellar kinematics and/or the stellar velocity dispersion significantly. Due to the expected intense star-forming activity of J0822+2241, its spectrum is expected to be dominated by its ionized interstellar medium with a negligible contribution from older stellar populations. Thus, we do not perform starlight subtraction since no significant absorption features are expected. After experimenting with a number of alternative models for the underlying continuum, we settled for a simple redshifted power-law model within PyXspec to constrain the pseudocontinuum. Since the pseudocontinuum model chosen is not physical and (as noted in Section 2) the signal-to-noise ratio of the continuum is far lower than the emission lines, we do not attempt to subtract the continuum to generate an emission-line-only spectrum. Instead, we leave our pseudocontinuum model free to vary during all emission-line fits, so that any emission-line parameter uncertainties naturally incorporate the uncertainty associated with the pseudocontinuum itself. We note that all reported Balmer emission-line fluxes could thus be underestimated in the event that substantial Balmer absorption is present, which is not accounted for with our pseudocontinuum model. For all emission-line fits, we used wide uniform and log-uniform priors for the pseudocontinuum power-law photon index and normalization with the zpowerlw model in PYXSPEC.

#### 3.2.1. Constructing a Narrow Line Template

On visual inspection, the H$\alpha$ $\lambda$6563 emission line appears to be significantly blended with the [N II] $\lambda\lambda$6548, 6583 doublet in the SDSS spectrum of J0822+2241. Thus, to deblend the [N II] doublet from H$\alpha$, we follow the technique of A. E. Reines et al. (2013; see also A. V. Filippenko & W. L. W. Sargent 1988, 1989; L. C. Ho et al. 1997; J. E. Greene & L. C. Ho 2004; X.-B. Dong et al. 2012; W.-J. Liu et al. 2025) by fitting the [S II] $\lambda\lambda$6716, 6731 doublet to produce a narrow component template for each of the

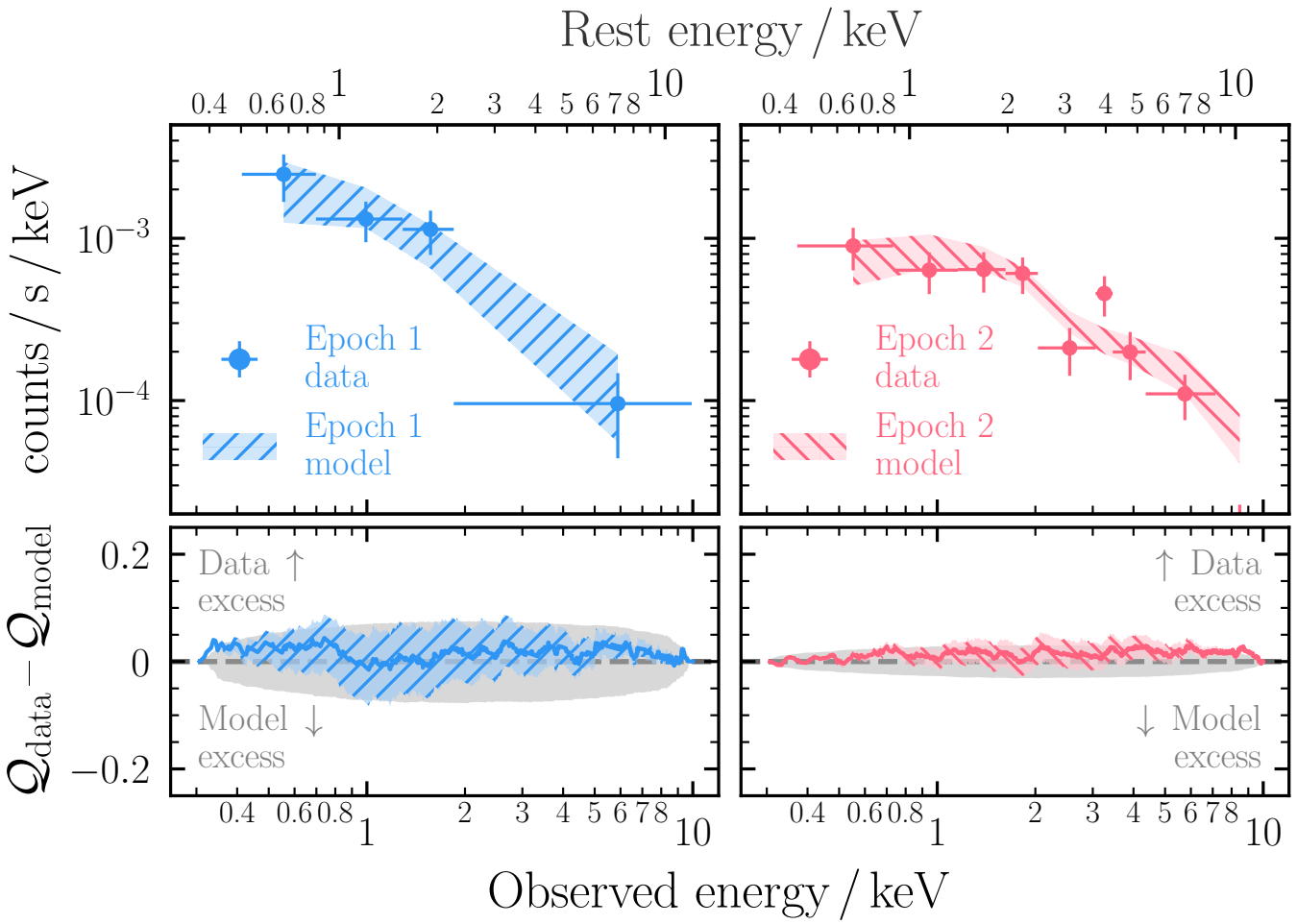


**Figure 1.** Independent spectral fits to epoch 1 (left) and epoch 2 (right) XMM-Newton data of J0822+2241. The model used for both epochs is a redshifted power law with fixed Galactic absorption, and the hatched shaded regions show the 90% model posterior uncertainty in all panels. The observed spectral shape is harder in epoch 2 than in epoch 1, driven predominantly by a drop in flux at energies $\lesssim$2 keV. The bottom panels show the quantile–quantile difference plots in which $\mathcal{Q}_{\rm data} - \mathcal{Q}_{\rm model}$ are plotted against energy (see Section 2 for more information). The background gray shaded regions represent the 90% posterior-predictive range derived by simulating a random selection of the posterior model rows many times with the same instrumental setup as the real data (i.e., the same background, response, and exposure time). Since the hatched shaded regions for both epochs agree with the gray shaded regions, we confirm that each model can explain the observed data in each epoch satisfactorily.

narrow [N II] lines, as well as the narrow component to the H$\alpha$. We trial two narrow-line models to fit [S II]. The first contains a single-Gaussian model per [S II] line (allowed to vary in width between 50 and 300 km s$^{-1}$), and the second contains two narrow Gaussian models (with the additional second Gaussians allowed to vary in width between 50 and 1000 km s$^{-1}$). It is important to note that some previous Gaussian decompositions of the [S II] complex within AGN SDSS spectra have required varying intensity ratios between each [S II] line (see, e.g., L. C. Ho et al. 1997 for examples), though typically in a minority of cases. However, we did not find that such additional complexity was required while fitting the [S II] doublet of J0822+2241, and thus the intensities of each [S II] line were tied together in all corresponding parameterizations.

We fit the [S II] doublet over the rest-frame wavelength range 6620–6850 Å[25] with a total (including the two pseudocontinuum model parameters) of five and seven free parameters in the 1-Gaussian and 2-Gaussian models, respectively. For the 1-Gaussian model we varied a single normalization and line width applied to each [S II] line with log-uniform priors, as well as the line centroid of [S II] $\lambda$6716 with a uniform prior, while enforcing that the relative separation of [S II] $\lambda$6716 and [S II] $\lambda$6731 was fixed to the laboratory value. The same priors were applied to the additional Gaussian lines used in the 2-Gaussian model, though with a wider allowable range in line width as specified above. The line centroid shift of both additional Gaussian lines was also tied to the value derived with the first Gaussian line model for [S II] $\lambda$6716.

Figure 3 presents the results from our spectral fits to the [S II] $\lambda\lambda$6716, 6731 complex of J0822+2241 with our 1-Gaussian and 2-Gaussian models. We find that a single Gaussian line is incapable of explaining the relatively broad base of either [S II] emission line (see the middle panel of Figure 3). The corresponding $\chi^2$ values for each spectral fit also favored the inclusion of two Gaussian lines to explain the [S II] doublet. We find an improvement in $\chi^2$ from 213.12 with 133 degrees of freedom ($\chi^2_n = 1.60$) to 133.99 with 131 degrees of freedom ($\chi^2_n = 1.02$) when using the 1-Gaussian and 2-Gaussian models to explain the [S II], respectively. The resulting 2-Gaussian model fit, highlighting the additional broader Gaussian component per [S II] line, is shown in the top

[25] On visual inspection, we identified a prominent emission line coincident with He I $\lambda$6678. Thus, for all fits encompassing this emission line, we excised the rest-frame 6678 ± 14 Å window from the spectrum.

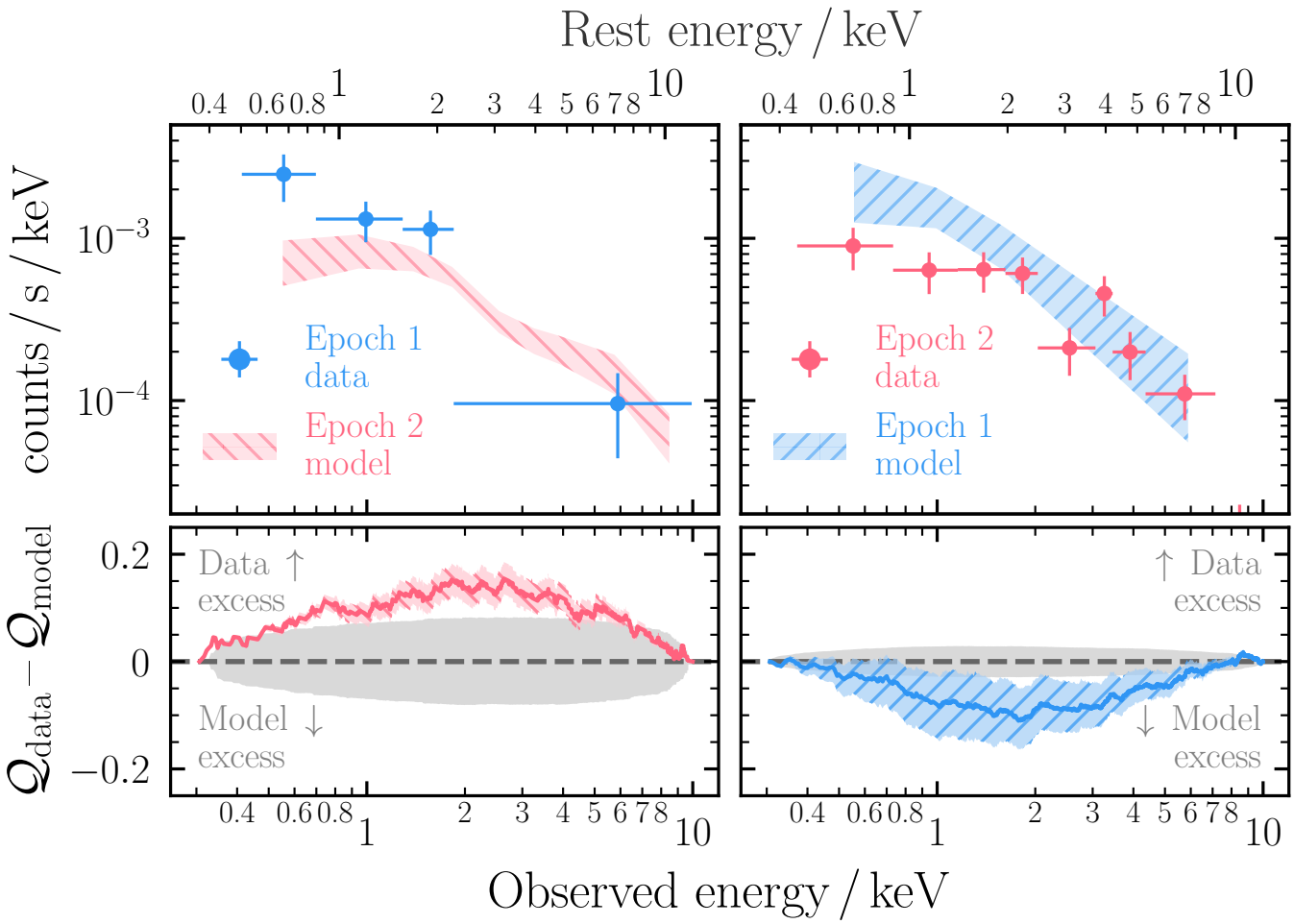


**Figure 2.** Same as Figure 1, except that the posterior model found for each epoch has been swapped to check whether the epoch 1 model can explain the data from epoch 2 and vice versa. The bottom panels that show the quantile–quantile difference plots are discrepant to the posterior-predictive range shown with gray shading. The hatched shaded bands give a peak and trough at ∼2 keV in the bottom left and right panels, respectively. Since the information conveyed is cumulative, the bottom left panel indicates that there is a significant excess in detected counts for epoch 1 relative to the model posterior prediction from epoch 2 (see Section 2 for more information). The opposite is true for the bottom right panel, in which the detected counts in epoch 2 are significantly suppressed relative to the model posterior from epoch 1. Given the excesses relative to the gray shaded regions in either panel, we conclude that the deviations $\lesssim$2 keV are significant to >90% confidence.

panel of Figure 3. Given the general lack of significant residuals in the bottom panel of Figure 3, we proceed with the 2-Gaussian model as a narrow-line template for the [N II] $\lambda\lambda$6548, 6583 doublet, as well as the narrow core of the H$\alpha$ $\lambda$6563 line.

### 3.2.2. *Characterizing the H$\alpha$ Complex*

As shown in the top panel of Figure 3, both components within the 2-Gaussian line template model display noticeable uncertainty within the posteriors of their model components. To self-consistently propagate all the information encompassed by these uncertainties into our final H$\alpha$ $\lambda$6563 emission-line constraints, we simultaneously fit the narrow-line template with the [S II] $\lambda\lambda$6716, 6731 doublet in combination with the [N II] $\lambda\lambda$6548, 6583 doublet and H$\alpha$ $\lambda$6563 emission line over the rest-frame 6400–7000 Å passband. We incorporate two models in total: (i) a baseline model in which the [N II] and [S II] doublets and H$\alpha$ $\lambda$6563 emission line are explained purely with our 2-Gaussian narrow-line template derived in Section 3.2.1, and (ii) the same baseline model with an additional broad Gaussian line component to the H$\alpha$ emission line included. The relative scaling between the two Gaussian components of each narrow line was tied to that of the [S II] doublet. To account for any asymmetries in the narrow H$\alpha$ emission line, we additionally allowed the line centroids of both components to vary uniformly by $\pm$10 Å. For the additional broad Gaussian line in model (ii), we allowed the normalization, width, and line centroid to vary as free parameters.

Figure 4 presents the results from our spectral fits with models (i) and (ii), focused on a zoom-in of the [N II] and H$\alpha$ emission-line complex. We found that the inflection points between H$\alpha$ and each [N II] line were not well reproduced using just the narrow-line template, resulting in strong residuals on either side of H$\alpha$ (see the middle panel of Figure 4). Using the narrow-line template resulted in a $\chi^2$ of 657.96 with 367 degrees of freedom ($\chi^2_n = 1.79$). The inclusion of an additional broad emission line component to H$\alpha$ in model (ii) provided a significant improvement to the spectral fit with a $\chi^2$ of 463.48 with 364 degrees of freedom ($\chi^2_n = 1.27$). The top and bottom panels of Figure 4 present the spectral fit with model (ii) and its corresponding residuals, respectively. The presence of the broad component significantly reduced the residuals on either side of the narrow component to H$\alpha$, as expected. We also find that the observed flux posterior of the component is monomodal and well constrained with $\log F_{\mathrm{H}\alpha,\,\mathrm{broad,obs}}/\mathrm{erg\,s^{-1}\,cm^{-2}} = -14.41^{+0.06}_{-0.05}$, implying that the component is significantly required within the

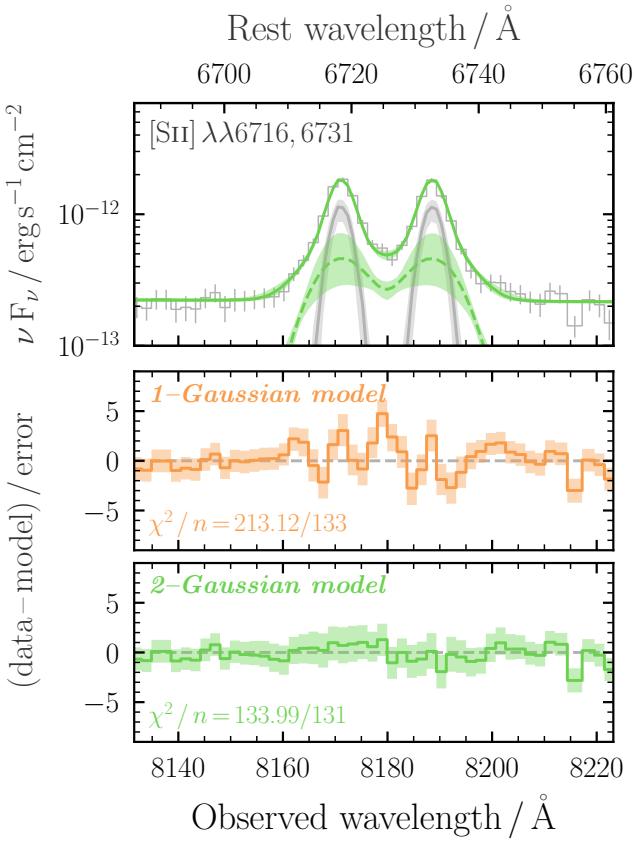


**Figure 3.** Top: [S II] λλ6716, 6731 doublet in the SDSS spectrum of J0822+2241, fit with the 2-Gaussian spectral model described in Section 3.2.1. The green solid line shows the total model, whereas the gray solid lines and green dashed line show the first and second Gaussian model components to each [S II] line, respectively. Middle: residuals from a separate fit with the 1-Gaussian model in which a single Gaussian component was used to explain each [S II] line. Bottom: residuals arising from the model with the 2-Gaussian model shown in the top panel. Given the improvement in reduced $\chi^2$, we use the 2-Gaussian model as a narrow emission line template for the [N II] λλ6548, 6583 doublet and narrow core of the Hα λ6563 emission line.

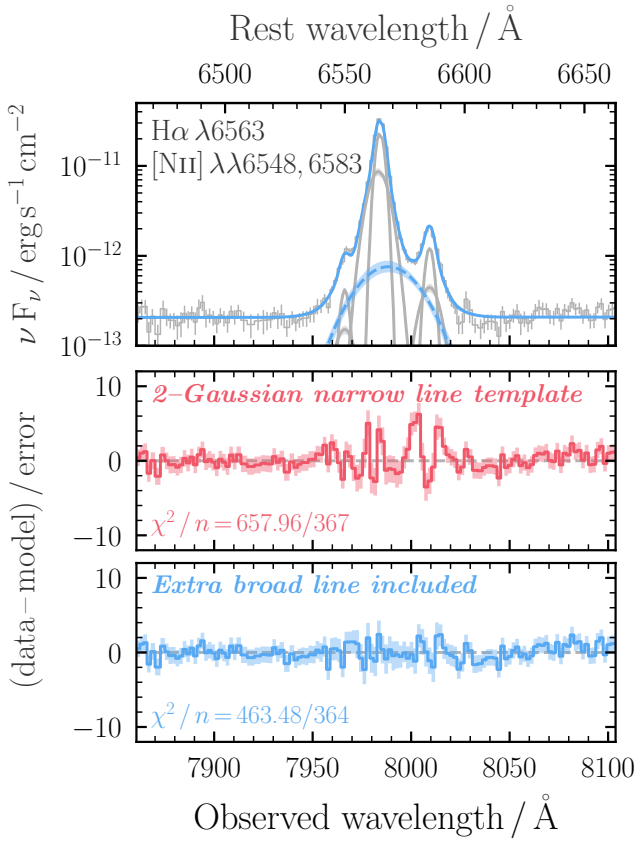


**Figure 4.** Top: SDSS Hα and [N II] complex of J0822+2241, with the spectral fit described in Section 3.2.2. The solid blue line shows the total model, and the dashed blue line with shaded region shows the posterior constraint on the broad component to Hα. The gray lines and associated shading show the posterior constraints on the narrow components to the [N II] doublet and Hα line using the narrow-line template derived in Section 3.2.1. Middle: residuals from a similar fit in which no broad component to Hα was included. Bottom: residuals arising from the model with a broad Hα line included, relevant to the spectral fit shown in the top panel.

parameterization of model (ii). The corresponding observed luminosity of the broad component to Hα is $\log L_{\mathrm{H}\alpha,\,\mathrm{broad,\,obs}}/\mathrm{erg\,s^{-1}} = 41.72^{+0.06}_{-0.05}$ with an $\mathrm{FWHM}_{\mathrm{H}\alpha,\,\mathrm{broad}} = 1360^{+70}_{-100}$ km s$^{-1}$, after correcting for Milky Way extinction (but before accounting for extinction intrinsic to J0822+2241—see Section 3.2.3).

Broad Hα with $\mathrm{FWHM}_{\mathrm{H}\alpha,\,\mathrm{broad}} \lesssim 2000$ km s$^{-1}$ has been shown previously to trace the broad-line region surrounding low-mass AGN (e.g., A. E. Reines et al. 2013; A. E. Reines & M. Volonteri 2015). However, broad components to Balmer lines are also known to be prevalent in low-mass and/or low-metallicity systems similar to J0822+2241, often attributed to the interaction between massive stars and their interstellar medium and/or supernova activity (e.g., Y. I. Izotov et al. 2007). Thus, care should always be taken in interpreting broad Balmer line components as purely AGN driven (see also R. Maiolino et al. 2025, for a recent overview). In the cases in which broad Balmer line emission is powered by a dominant contribution from massive stars, the equivalent width of the broad component is typically $\lesssim$20 Å (Y. I. Izotov et al. 2007; F. Martins et al. 2020). For our spectral fit to J0822+2241, the equivalent width of the broad component to Hα is $\mathrm{EW}_{\mathrm{H}\alpha,\,\mathrm{broad}} = 90^{+12}_{-10}$ Å, suggesting an origin purely from massive stars to be unlikely (though not impossible).

On the other hand, powerful broad Hα emission is commonly seen in core collapse and/or superluminous supernovae (e.g., C. P. Gutiérrez et al. 2017) and typically decays on timescales of several years at most. As a rudimentary test of a supernova origin to the broad Hα component we detect in J0822+2241, we obtained updated Palomar/DoubleSpec spectroscopy of J0822+2241 ∼20 yr (∼16 yr in rest frame) after the original SDSS spectrum was taken. The corresponding comparison between the [S II] λλ6716, 6731 doublet, the [N II] λλ6548, 6583 + Hα λ6563 complex, and the Hβ λ4861 line is presented in the Appendix and Figure A1, in which the line profiles are remarkably similar across the ∼16 yr baseline within expected calibration-based systematic uncertainties.

Thus, based on the evidence we have in hand, it is likely that the broad Hα line identified in J0822+2241 is powered by the broad-line region surrounding an AGN (see also C. Simmonds et al. 2016). Future observations (e.g., time-resolved spectroscopy and/or resolved integral field unit observations) would be required to definitively prove that the broad Hα component is indeed AGN powered.

### 3.2.3. Estimating Extinction with the Balmer Decrement

To access the intrinsic broad Hα λ6563 flux measured from the SDSS spectrum of J0822+2241, we additionally measure the line-of-sight extinction from the Hβ λ4861 emission line using the Balmer decrement. Since we find evidence for a

significant broad component to the H$\alpha$ emission line, it is plausible a priori that a broad component to H$\beta$ exists. However, due to our use of a simple pseudocontinuum model, we cannot easily rely on the same [S II] narrow-line template to account for the narrow component to the H$\beta$ line, which would strictly require the same power law to explain the continuum over $\gtrsim$1500 Å between the [S II] doublet and H$\beta$. Previous analyses of AGN candidates have focused on using the [O III] emission lines to provide a narrow-line template for H$\beta$ (e.g., W.-J. Liu et al. 2025). However, Green Pea galaxies are defined to have extremely bright and complex [O III] emission, often including prominent broad components (e.g., Y. I. Izotov et al. 2011). Thus, we purposefully avoid using [O III] to interpret the narrow component of H$\beta$, and instead we fit the H$\beta$ line by itself over the rest-frame wavelength range 4750–4950 Å.

Figure 5 presents our phenomenological fitting to the H$\beta$ line. The fitting process is analogous to our spectral fitting of the [S II] doublet in Section 3.2.1, in which we trial a single-Gaussian model for the H$\beta$ line, followed by a double-Gaussian model. For the single-Gaussian line model, the continuum slope and normalization, as well as the line centroid, width, and normalization, were allowed to vary, giving five free parameters. For the double-Gaussian model, the line centroid, width, and normalization of both components were allowed to vary freely, giving eight free parameters. We clearly find that the 1-Gaussian model is incapable of fitting the relatively broad base of the H$\beta$ emission line (see the middle panel of Figure 5), giving a $\chi^2$ of 533.39 with 172 degrees of freedom ($\chi^2_n = 3.10$). Including the extra Gaussian component in the 2-Gaussian model substantially improves the fit, giving a $\chi^2$ of 168.69 with 169 degrees of freedom ($\chi^2_n = 0.99$). However, we find that the second (broader) Gaussian component has a width of $\mathrm{FWHM}_{\mathrm{H}\beta,\ \mathrm{component\ 2}} = 500 \pm 20\ \mathrm{km\ s^{-1}}$, which is insufficiently broad to have a high likelihood of being AGN powered. Given the lack of a component comparably broad to the broad component of H$\alpha$, we make the conservative assumption that the total flux of both components composing the H$\beta$ emission line constitutes the narrow H$\beta$ flux used to derive the Balmer decrement, which equates to $\log F_{\mathrm{H}\beta,\ \mathrm{narrow,obs}} = -14.08 \pm 0.01$, after correcting for Milky Way extinction.

The corresponding Balmer decrement arising from the ratio between the narrow H$\alpha$ and H$\beta$ fluxes is $F_{\mathrm{H}\alpha,\ \mathrm{narrow,obs}}/F_{\mathrm{H}\beta,\ \mathrm{narrow,obs}} = 4.2 \pm 0.6$. We translate the observed Balmer decrement into a nebular color excess value of $E(B-V) = 0.3 \pm 0.1$ mag for J0822+2241 using Equation (4) of A. Domínguez et al. (2013) with the reddening law of D. Calzetti et al. (2000) assuming an intrinsic H$\alpha$/H$\beta$ ratio of 2.86 (D. E. Osterbrock 1989). Again using D. Calzetti et al. (2000), we estimate the extinction at rest-frame H$\alpha$ to provide an intrinsic absorption-corrected broad H$\alpha$ luminosity of $\log L_{\mathrm{H}\alpha,\ \mathrm{broad,int}}/\mathrm{erg\ s^{-1}} = 42.1^{+0.3}_{-0.2}$.

### 3.3. Spectral Energy Distribution Analysis

In the left panel of Figure 6, we show the X-ray to infrared broadband SED for J0822+2241, along with model constraints from `Lightning`. Our models prefer a solution in which both stellar and AGN processes are important in different regimes. For instance, stellar emission is expected to be important in the UV-to-optical regime and to potentially dominate at wavelengths longer than ~10 $\mu$m owing to cold dust emission. In contrast, an AGN component is required to dominate the

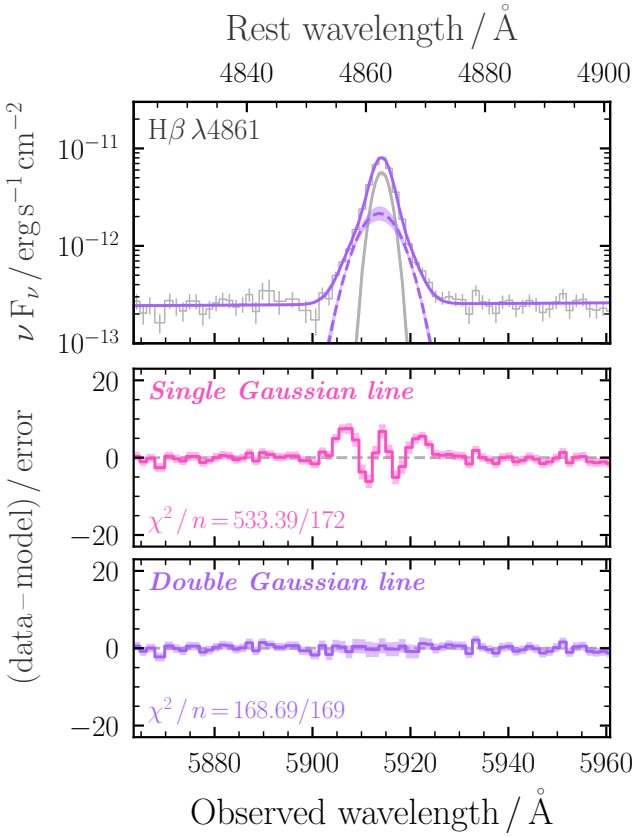


**Figure 5.** Top: SDSS H$\beta$ $\lambda$4861 emission line of J0822+2241, with the spectral fit described in Section 3.2.2. The solid purple line shows the total model, and the dashed purple line with shaded region shows the posterior constraint on the second Gaussian component to H$\beta$. The gray line and associated shading show the posterior constraint on the first narrower Gaussian component to the H$\beta$ line. Middle: residuals from an equivalent fit using a single Gaussian component. Bottom: residuals arising from the model with an additional Gaussian component to the H$\beta$ line included, relevant to the spectral fit shown in the top panel.

detected X-ray emission, with potentially important contributions to the UV-to-optical regime, and to dominate the ~3–10 $\mu$m near-to-mid-infrared regime. It is useful to also note that the total infrared SED encompassed by the four-band WISE photometry is characteristically steep, as previously identified by T. Kawamuro et al. (2019), but `Lightning` is able to predict that the red spectral shape is a result of AGN *and* host galaxy processes.

We find the corresponding galaxy parameter posteriors derived with `Lightning` to be in basic agreement with those derived in the literature for J0822+2241 from the optical and UV portions of its SED. However, on average we find larger uncertainties owing to the requirement for a joint contribution to the UV-to-optical regime from AGN and stellar processes. Specifically, we constrain the average star formation rate over the past 10 Myr to be $\mathrm{SFR}_{t<10\ \mathrm{Myr}} = 44^{+50}_{-38}\ M_\odot\ \mathrm{yr}^{-1}$ and the integrated galaxy stellar mass to be $M_* = 1.8^{+0.8}_{-1.5} \times 10^{10}\ M_\odot$.

For the AGN component, the X-ray and near-to-mid-infrared data are able to place some constraints on black hole mass using the parameterization within the `qsosed` model, finding $M_{\mathrm{BH}} = 1.2^{+2.5}_{-0.2} \times 10^6\ M_\odot$. Combined with the constraint on stellar mass, `Lightning` predicts J0822+2241 to lie far closer to the stellar mass versus black hole mass relation derived for typical broad-line dwarf AGN from A. E. Reines & M. Volonteri (2015) (see Figure 7). As described in Section 4,

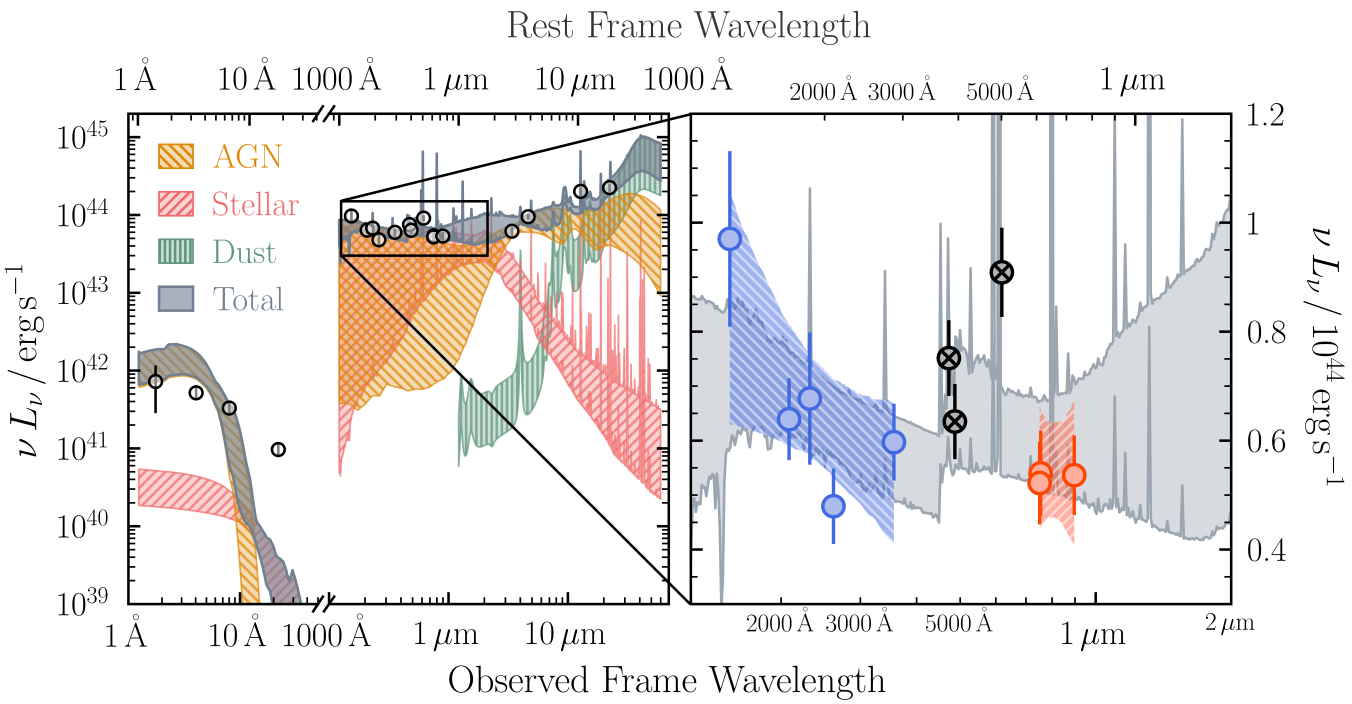


**Figure 6.** Left: broadband SED of J0822+2241 (black circles with associated 68% error bars), fit with the `Lightning` software package. The total model is shown with a dark-gray shaded region, whereas the constituent AGN, attenuated stellar, and dust components are shown with hatched golden, red, and green regions, respectively. The left-hand portion of the plot shows the `Lightning` fit to the XMM-Newton data of epoch 2. Right: a zoom-in of the UV-to-near-infrared portion of the SED. By fitting slopes to the spectrum blueward and redward of the Balmer break, we constrain the overall UV and optical slopes, akin to D. D. Kocevski et al. (2024), to compare to the expected spectral shape from Little Red Dots. All photometry blueward of the Balmer break is used to derive the UV slope, given by the hatched blue region. Redward of the Balmer break, substantial emission-line contamination from [O II] λλ3726, 3729 and [O III] λλ4959, 5007 is expected, such that we fit the optical slope between a restricted observed wavelength range of ∼7000–9000 Å. The corresponding optical spectral slope range constrained is shown with a red hatched region.

the addition of an AGN component can drastically alter the predicted stellar mass in a nonobvious manner, meaning that the true value may lie anywhere between the value derived by Y. I. Izotov et al. (2011) and that from our `Lightning` fit. The SED fitting additionally yields an AGN line-of-sight obscuring column density of $\log N_{\rm H}/{\rm cm}^{-2} = 22.7^{+u}_{-0.1}$, which is significantly larger than that determined from the X-ray data alone.

As shown on the left-hand side of the left panel of Figure 6, the `Lightning` solution leaves an elevated residual in the X-ray band at $\lesssim$1 keV. Some portion of the soft X-ray emission is modeled with stellar emission from X-ray binaries, which have a different absorption prescription to the AGN. At present the `Lightning` models are expected to underpredict the X-ray emission in the soft X-ray region of the SED, as it does not include emission from hot gas, nor does it include a metallicity dependence on the X-ray binary component. Recent studies have shown that X-ray binary emission is significantly elevated in low-metallicity environments and may plausibly be a factor of ≈3–5 times higher than our model predictions for J0822+2241, due to its relatively low metallicity (see, e.g., B. D. Lehmer et al. 2024; E. Kyritsis et al. 2025). Nonetheless, such a soft X-ray enhancement would still be insufficient to explain the broadband X-ray spectrum without a dominant contribution from an AGN, in agreement with our detailed X-ray fits of the XMM-Newton data. We note that performing the above SED fitting using the X-ray data from epoch 1, instead of epoch 2, yields consistent results for SFR $_{t<10\,{\rm Myr}}$, $M_{\rm BH}$, $M_*$, and $N_{\rm H}$, albeit with weaker constraints due to the lower signal-to-noise data.

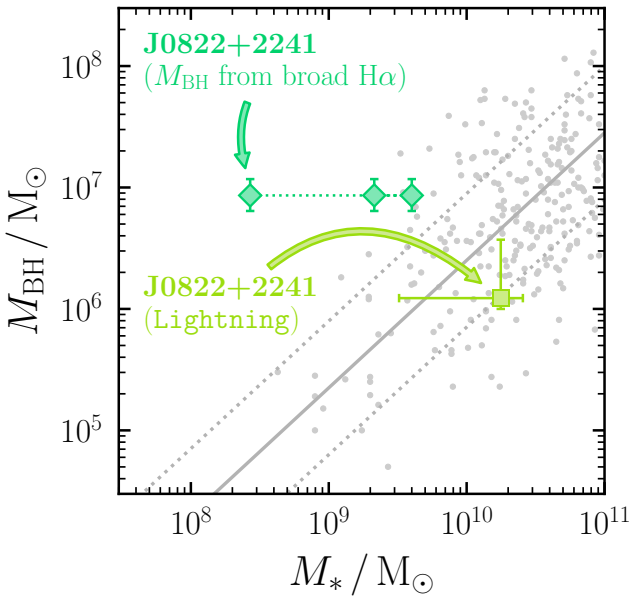


**Figure 7.** The local broad-line dwarf AGN sample with corresponding best-fit relation and intrinsic scatter between stellar mass and black hole mass from A. E. Reines & M. Volonteri (2015). The black hole mass measured for J0822+2241 using the broad Hα component identified in the SDSS optical spectrum (see Section 5.1) is overplotted with a green diamond, together with three literature values of stellar mass taken from Y. I. Izotov et al. (2011), C. Cardamone et al. (2009), G. Kauffmann et al. (2003), and J. Brinchmann et al. (2004) shown with the left, middle, and right diamonds, respectively. The alternative black hole versus stellar mass derived from `Lightning` that considers the presence of an AGN (see Section 3.3) is shown with a lighter-green square.

### 3.4. The UV-to-optical Spectral Shape

R. Lin et al. (2025) recently showed that a subset of Green Pea galaxies hosting broad permitted Balmer lines have "V"-shaped continua in $\nu F_\nu$ space in close analogy to Little Red Dots, following the spectral slope parameterizations of D. D. Kocevski et al. (2024). A remaining question from our broadband SED fitting of J0822+2241 is thus whether or not the underlying continuum shape in the UV-to-optical regime is consistent with that of Little Red Dots. To test this possibility, we consider the spectral slopes on either side of the Balmer break in the rest-frame wavelength ranges of 1000–3645 Å and 3645 Å – 1 $\mu$m for the UV and optical spectral slopes, respectively. All spectral slopes were derived by fitting a linear relation between logarithmic observed wavelength and observed flux density in AB magnitudes assuming $m_{\rm AB} = -2.5(\beta + 2)\log\lambda + c$, where $\beta$ is the spectral slope (D. D. Kocevski et al. 2024). The linear relation was fit using `UltraNest`, assuming a uniform prior for the gradient from −10 to 10 and log-uniform priors for the $y$-intercept and intrinsic scatter in the $y$-direction ranging from 0.1 to 100 and from 0.001 to 1, respectively.

The corresponding UV slope derived by fitting five photometry points blueward of the Balmer break (see the right panel of Figure 6) is $\beta_{\rm UV} = -1.5^{+0.4}_{-0.7}$, which satisfies the D. D. Kocevski et al. (2024) little red dot UV slope requirement of $\beta_{\rm UV} < -0.37$. By comparing the optical photometry for J0822+2241 with the predicted `Lightning` fit, there is expected spectral line contamination from [O II] $\lambda\lambda$3726, 3729 and [O III] $\lambda\lambda$4959, 5007. We thus excluded the photometry associated with those lines from our spectral slope estimates. The corresponding slope measured between the three optical photometric points shown in Figure 6 is $\beta_{\rm optical} = -1.3^{+2.5}_{-2.2}$. Clearly, even though the slope measurement is consistent with the D. D. Kocevski et al. (2024) requirement of $\beta_{\rm optical} > 0$, the uncertainties are substantial owing to the lack of reliable photometry to estimate the spectral slope from. The predicted `Lightning` model >1 $\mu$m clearly increases on average to reproduce the red near-to-mid-infrared WISE photometry, but the observed optical spectrum appears to be inconsistent with Little Red Dots.

## 4. Estimating the Black Hole and Host Galaxy Stellar Masses

Two important parameters to consider for J0822+2241 in light of the presence of broad H$\alpha$ and our broadband SED fits are the black hole and host galaxy stellar masses. For example, previous work has found evidence suggesting that compact low-mass galaxies with broad permitted optical lines host "overmassive" central black holes, with black hole masses exceeding predictions from scaling relations depending on stellar mass (e.g., I. Juodžbalis et al. 2025; R. Lin et al. 2025). Such an overmassive scenario could hint toward previous episodes of prolonged rapid black hole growth. However, the stellar mass of luminous compact galaxies such as J0822+2241 is notoriously difficult to measure, due in part to the requirement for a correct treatment of ionized gas emission, as well as the general difficulty associated with characterizing old stellar populations (see, e.g., Section 5 of Y. I. Izotov et al. 2011). In total, we consider three stellar mass measurements for J0822+2241 derived with different methods from G. Kauffmann et al. (2003), J. Brinchmann et al. (2004), C. Cardamone et al. (2009), and Y. I. Izotov et al. (2011), yielding stellar masses of $M_* = 4\times10^9\,M_\odot$, $2\times10^9\,M_\odot$, and $3\times10^8\,M_\odot$, respectively. The stellar mass of G. Kauffmann et al. (2003) and J. Brinchmann et al. (2004) was measured by multiplying its dust- and $K$-corrected $z$-band luminosity by a $z$-band mass-to-light ratio estimation, whereas C. Cardamone et al. (2009) measured stellar masses by convolving the observed SDSS spectral continuum with 19 medium-band filters and fitting stellar population models with the observed GALEX UV data. C. Cardamone et al. (2009) note that, due to the difficulty associated with properly accounting for older stellar populations, a minimum systematic uncertainty of 0.3 dex should be considered. By considering the contribution from stellar and ionized gas emission, Y. I. Izotov et al. (2011) fit the full SDSS spectrum (continuum and lines) of J0822+2241 assuming a recent burst of star formation combined with a prior continuous and constant episode of star formation. The substantially smaller stellar mass than G. Kauffmann et al. (2003), J. Brinchmann et al. (2004), and C. Cardamone et al. (2009) derived is due to the extra contribution from gaseous continuum emission that is accounted for by Y. I. Izotov et al. (2011).

To derive a black hole mass for J0822+2241, we first consider our absorption-corrected broad H$\alpha$ luminosity and FWHM from Section 3.2.3, together with the black hole mass relation given in Equation (5) of A. E. Reines et al. (2013). The corresponding black hole mass found for J0822+2241 from the broad H$\alpha$ line is $M_{\rm BH,H\alpha} = 8^{+3}_{-2}\times10^6\,M_\odot$, though we note that this mass prediction does fundamentally rely on an extrapolation from more luminous AGN that may not hold for low-metallicity systems such as Green Pea galaxies (see Section 3.5 of A. E. Reines et al. 2013 for further discussion). Figure 7 presents the H$\alpha$-based black hole mass for J0822+2241 together with all three stellar masses overplotted on the black hole mass versus stellar mass scaling relation of A. E. Reines & M. Volonteri (2015).

On first interpretation, the H$\alpha$-based black hole mass estimation found for J0822+2241 lies significantly outside the intrinsic scatter of A. E. Reines & M. Volonteri (2015) for all literature stellar masses, though the most extreme offset is found with the stellar mass of Y. I. Izotov et al. (2011). However, all literature methods selected do not consider an additional contribution from an AGN. If the observed optical continuum of J0822+2241 were also found to include a contribution from an AGN (as suggested by our `Lightning` SED fits), the stellar masses derived could have significant uncertainties that are not shown in Figure 7 (see J. Buchner et al. 2024 for a detailed discussion of AGN-induced stellar mass uncertainties). On one hand, if the AGN emission were to make the object brighter in all bands without adding significant color terms, the current stellar masses could be considered upper limits. A smaller stellar mass would then make J0822+2241 more of an outlier compared to the A. E. Reines & M. Volonteri (2015) relation. On the other hand, if the contribution from an AGN were to make the observed continuum bluer without significantly affecting the total flux in the redder bands, the contribution from younger stellar populations could be overestimated. As younger stellar populations have a lower mass-to-light ratio, the stellar masses could then be considered as lower limits.

For completeness, we additionally plot the self-consistently derived black hole and stellar masses derived from

Lightning. Though the uncertainties are larger, the masses derived with Lightning are consistent with the stellar mass versus black hole mass relation of A. E. Reines & M. Volonteri (2015). Our Lightning SED fits thus suggest that there is a plausible parameterization that includes an AGN in which the black hole mass is not overmassive relative to the stellar mass scaling relation of A. E. Reines & M. Volonteri (2015). We thus conclude that the current evidence is insufficient to make any strong claims that depend on the stellar mass of J0822+2241.

## 5. Discussion

Given the observed X-ray, optical, and broadband SED properties of J0822+2241, we now consider three physical scenarios to explain the primary X-ray power source.

### 5.1. Obscured X-Ray Emission from an AGN

A natural explanation for a persistent 2–10 keV luminosity of $\sim 10^{42}\,\mathrm{erg\,s^{-1}}$ combined with decreasing soft X-ray luminosity over a baseline of 6.2 yr is from obscuration changes surrounding a Seyfert-like AGN. The vast majority of AGN are known to be obscured (e.g., Y. Ueda et al. 2014; J. Buchner et al. 2015; C. Ricci et al. 2017a; N. Torres-Albà et al. 2021; A. Tanimoto et al. 2022; P. G. Boorman et al. 2025), and soft X-ray signatures of obscuration changes have been confirmed in numerous previous studies of the local Seyfert population (e.g., G. Risaliti et al. 2002; E. Rivers et al. 2011; A. G. Markowitz et al. 2014; D. J. Walton et al. 2014; M. Lefkir et al. 2023; N. Torres-Albà et al. 2023; A. Pizzetti et al. 2025). Specifically in the case of J0822+2241, changing photoelectric absorption could deplete the 0.5–2 keV flux between epochs 1 and 2 without significantly altering the harder 2–10 keV flux, resulting in a spectral hardening akin to that found in Section 3.

We fit an absorbed power law (zTBabs*cabs*zpowerlw in Xspec parlance) to both epochs simultaneously while allowing the line-of-sight column density to vary independently between epochs. The resulting spectral fits with folded posterior ranges are shown in the left panel of Figure 8. Both epochs are explained well by the model, resulting in an observed-frame 2–10 keV flux of $\log F_{2-10\,\mathrm{keV}}/\mathrm{erg\,s^{-1}\,cm^{-2}} = -14.0 \pm 0.1$ and intrinsic photon index of $\Gamma = 1.7^{+0.1}_{-0.2}$, fully consistent with the typical photon index values found from surveys of AGN (e.g., C. Ricci et al. 2017a). We find line-of-sight column densities of $\log N_{\mathrm{H}}/\mathrm{cm^{-2}} = 20.7^{+0.7}_{-u}$ and $21.8 \pm 0.3$ for epochs 1 and 2, respectively. Our use of BXA enables us to propagate the posteriors of column density per epoch into a single posterior on the column density ratio between each epoch that, by design, incorporates all covariance associated with the fit. By integrating the probability mass encompassed in the epoch 2/epoch 1 column density ratio posterior with values above unity, we find that an increase in obscuration between 2013 and 2020 is required to >99.8% confidence. In case integrating the posterior derived from UltraNest is affected by discrete sampling effects, we additionally fit the column density ratio posterior with a flexible beta function following the method of L. Baronchelli et al. (2020). The corresponding one-dimensional posterior and beta function fit are shown in the right panel of Figure 8, in which the probability of an increase in obscuration between 2013 and 2020 is required to >99.7% confidence. The beta function fit additionally yields a fractional column density increase of $\log(N_{\mathrm{H,2}}/N_{\mathrm{H,1}}) = 1.08^{+0.66}_{-0.72}$. We note that since the column density in epoch 1 is consistent with being below the Galactic value (i.e., unconstrained at the lower end), our column density ratio between epochs 2 and 1 and the corresponding probability for an increase in column density can both conservatively be considered lower limits.

To constrain the Eddington ratio in the obscured AGN scenario, we first estimate the bolometric luminosity using the relation between bolometric correction and 2–10 keV luminosity for AGN presented by F. Duras et al. (2020). Combined with the 2–10 keV luminosity constrained for J0822+2241, we find a bolometric correction of $\kappa_{\mathrm{X}} = 15.5 \pm 0.1$, which together give a bolometric luminosity of $L_{\mathrm{bol}}/\mathrm{erg\,s^{-1}} = 43.2 \pm 0.1$. By combining the H$\alpha$-derived black hole mass and bolometric luminosity estimates, we compute an Eddington ratio for J0822+2241 of $\lambda_{\mathrm{Edd}} = 1.4^{+0.4}_{-0.7}$ % ($\log \lambda_{\mathrm{Edd}} = -1.8^{+0.1}_{-0.2}$). Interestingly, the Eddington ratio range constrained is consistent with the effective Eddington limit on dusty gas (see A. C. Fabian et al. 2008; C. Ricci et al. 2017b). Previous work has shown the effective Eddington limit on dusty gas to coincide with a sharp decline in the fraction of obscured AGN selected within the 70-month Neil Gehrels Swift/BAT survey (C. Ricci et al. 2017b; T. T. Ananna et al. 2022; C. Ricci et al. 2022, 2023), consistent with a radiation-pressure-dependent covering factor of (sub-Compton-thick) material. If the same principle were to apply for J0822+2241, the obscuration change observed between epochs 1 and 2 could have arisen from an outflowing configuration.

### 5.2. Unobscured X-Ray Emission from an AGN

Soft X-ray variability is commonly observed in unobscured AGN (e.g., E. Kara & J. García 2025, and references therein), though the properties observed for J0822+2241 are largely disparate from the broader unobscured population. For example, a possibility to consider for the soft X-ray emission of J0822+2241 is a variable soft excess component that is often observed in unobscured AGN (e.g., M. Gierliński & C. Done 2004; J. Crummy et al. 2006; C. Done et al. 2012; D. J. Walton et al. 2013; A. Madathil-Pottayil et al. 2024; S. G. H. Waddell et al. 2024). In such a scenario the intrinsic photon index of the AGN coronal continuum would be harder than observed owing to the contribution of the soft excess flux at $\lesssim$2 keV. The most conservative scenario in producing the softest possible intrinsic photon index for J0822+2241 would be for the epoch 2 spectrum to feature no detectable soft excess. However, the observed photon index of the spectrum in epoch 2 ($\Gamma = 0.8^{+0.2}_{-0.3}$) is already considerably harder than is typically observed for unobscured AGN that are found to host strong soft excesses (e.g., C. Jin et al. 2012b), even before accounting for any potential soft excess in the fits to J0822+2241.

An alternative scenario to explain the power source of J0822+2241 is variable accretion onto an unobscured intermediate-mass black hole that has low enough mass for the accretion disk spectrum to be detectable by XMM-Newton. The observed photon index of J0822+2241 in epoch 2 ($\Gamma = 0.8^{+0.2}_{-0.3}$) is already significantly harder than the photon index found in one of the hardest states of ESO 243–49 HLX-1 ($\Gamma = 1.6 \pm 0.4$; M. Servillat et al. 2011), which is widely regarded as a strong intermediate-mass black hole candidate.

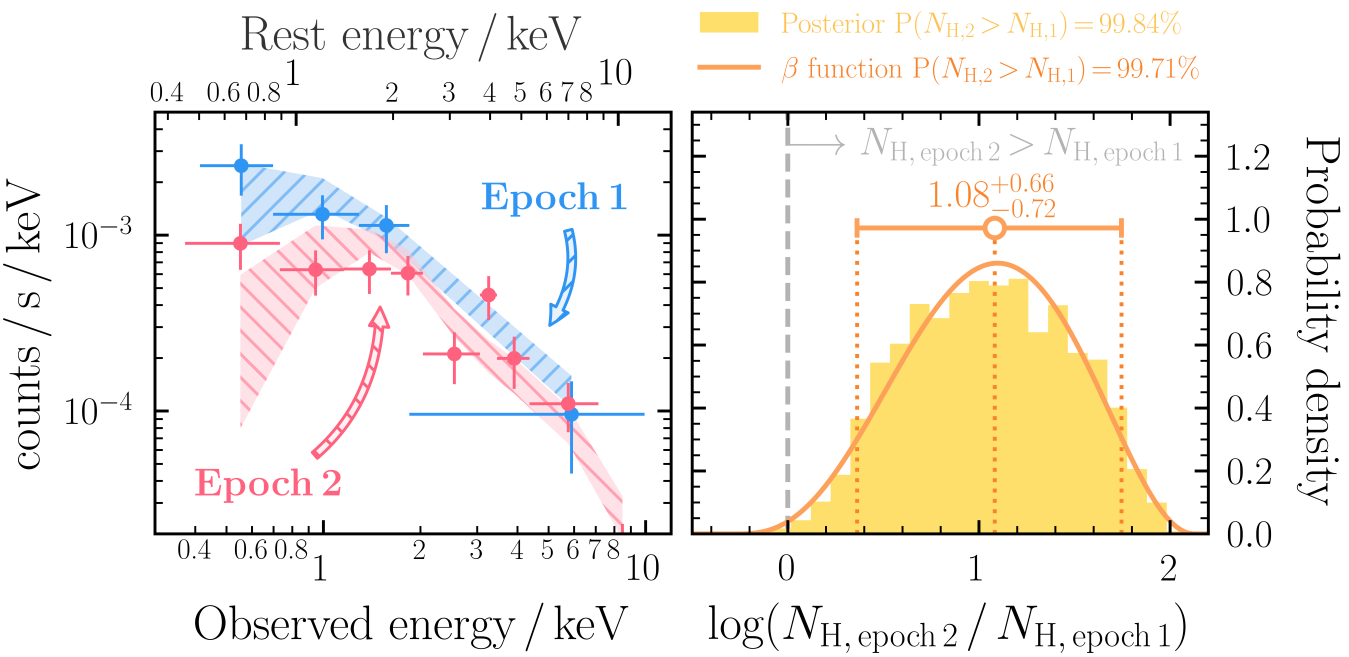


**Figure 8.** Left: simultaneous X-ray spectral fit to the two epochs of data from J0822+2241 using a redshifted power law with variable line-of-sight obscuration between epochs. Right: posterior distribution for the logarithmic ratio of column density from epoch 2 to epoch 1. All values above zero are consistent with the column density increasing from epoch 1 to epoch 2. The solid dark-orange curve shows an analytical beta function fit to the posterior distribution. Both the raw posterior and beta function agree that an increase in column density is required to >99.7% probability.

We therefore defined the minimum 0.5–2 keV flux of an accretion disk component to be the difference in flux between both epochs. Assuming upper limits for detectable accretion disk emission in the observed ultraviolet (as measured by the XMM-Newton/Optical Monitor UVW1 filter; M. J. Page et al. 2012) and 2–10 keV bands, we simulated accretion disk spectra with the KYNbb model (M. Dovčiak et al. 2008, 2004) while simultaneously varying black hole mass, spin, inclination, inner disk radius, and accretion rate. We find a black hole mass of $M_{\rm BH} = 1.1^{+36.0}_{-0.9} \times 10^4\,M_\odot$ (16th, 50th, and 84th percentiles), which is broadly consistent with the expectations from the stellar mass versus black hole mass scaling relation of A. E. Reines & M. Volonteri (2015) plotted in Figure 7. However, the black hole mass is significantly lower than the value derived using the broad H$\alpha$ emission line (see Section 3.2). Furthermore, the accretion rate would need to be super-Eddington, with $\dot{m} > \dot{m}_{\rm Edd}$, which in the literature to date has tended to be associated with substantially steeper spectra than the $\Gamma = 0.8^{+0.2}_{-0.3}$ observed in epoch 2 for J0822+2241. The properties of accreting compact objects at such large accretion rates are also not yet fully understood, but they are likely associated with powerful accretion disk winds that would render our use of KYNbb insufficient to constrain the black hole mass in the first place (A. King et al. 2023). Though undoubtedly an exciting possibility, we thus consider an unobscured intermediate-mass black hole revealed from X-ray spectral variability for J0822+2241 to be unlikely.

### 5.3. Off-nuclear Contaminants

As discussed in Section 1, B. Adamcová et al. (2024) have shown previously that J0822+2241 could not have a contribution of >20% to the total observed 0.5–8 keV luminosity from unresolved populations of X-ray binaries. Due to the consistent 2–10 keV luminosity between the two epochs, an individual short-term transient event producing the observed X-ray spectra such as a supernova is also effectively ruled out (e.g., V. V. Dwarkadas 2014). In addition, more X-ray-luminous supernovae are often accompanied by more rapid X-ray flux declines (V. V. Dwarkadas & J. Gruszko 2012). Thus, the cumulative effect from a sufficiently high frequency of supernovae to appear as a constant X-ray flux over ~6 yr in rest frame is additionally infeasible.

Due to the small physical size of J0822+2241 with an NUV half-light radius of 680 pc (H. Yang et al. 2017), the host galaxy is unresolvable by XMM-Newton. Thus, a remaining possibility to consider is that the X-ray emission we see from J0822+2241 arises from an unresolved number of ultraluminous X-ray sources (ULXs; $L_{\rm X} > 10^{39}$ erg s$^{-1}$; see A. King et al. 2023 for a review) and/or hyperluminous X-ray sources (HLXs; $L_{\rm X} > 10^{41}$ erg s$^{-1}$; Y. Gao et al. 2003). Figure 9 shows the observed X-ray luminosity of J0822+2241 in three bands from the individual epoch fitting with a power law detailed in Section 3. Each measured rest-frame observed luminosity is compared to the peak luminosities seen in the multimission catalog of ULXs derived by D. J. Walton et al. (2022) from the fourth XMM-Newton serendipitous source catalog (4XMM-DR10; N. A. Webb et al. 2020), the Neil Gehrels Swift X-Ray Telescope Point-source Catalog (2SXPS; P. A. Evans et al. 2020), and the Chandra Source Catalog DR2 (CSC2.0; I. N. Evans et al. 2020) in the left, middle, and right panels, respectively. The luminosities observed for J0822+2241 in both epochs are clearly extreme for individual members of the ULX population. Even though there is agreement with a small handful of sources identified to have peak luminosities in the 2SXPS survey consistent with J0822+2241, we note that the consistent 2–10 keV luminosity over 6.2 yr suggests that the measured luminosities are not peak luminosities in the first place.

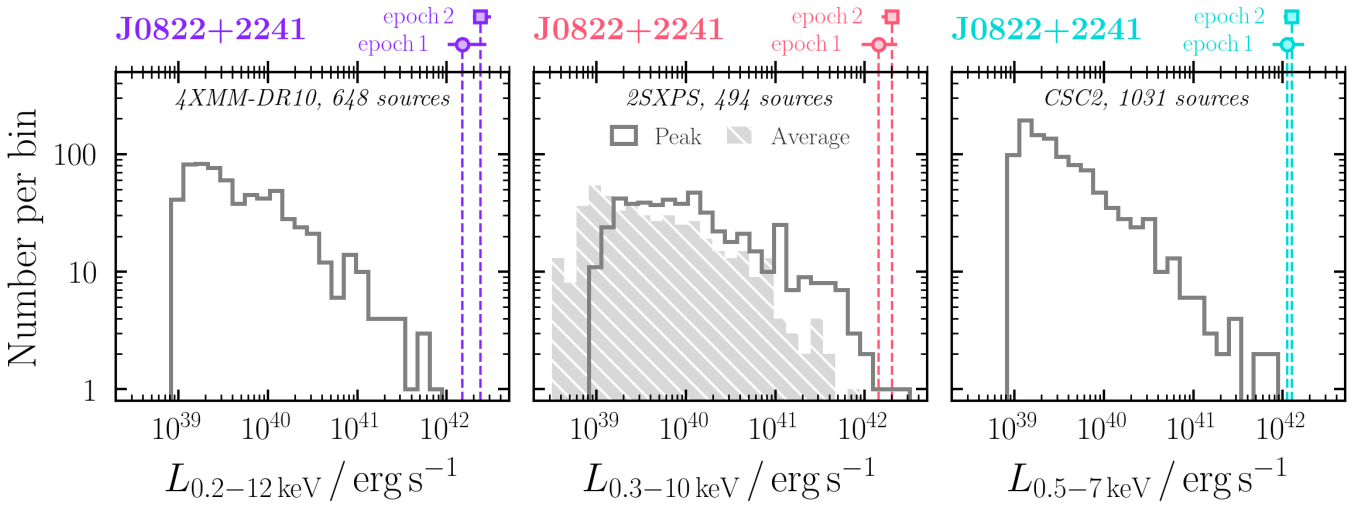


**Figure 9.** Each panel shows the observed luminosities of J0822+2241 measured with a `diskbb + diskpbb` model in different bands, compared to the distributions of peak luminosity found by D. J. Walton et al. (2022) for the ULX population in each of 4XMM-DR10 (left), 2SXPS (middle), and CSC2 (right). Since luminosities are reported for different default passbands per instrument, we note that the J0822+2241 luminosities plotted per panel are measured for different passbands to allow a direct comparison. Clearly J0822+2241 is a significant outlier, with only one source being consistent with the epoch 2 luminosity measurement of J0822+2241 in the 2SXPS peak luminosity distribution.

Though just contained within the populations plotted in Figure 9, current confirmed HLXs are considerably rarer (A. D. A. MacKenzie et al. 2023). As discussed in Section 5.2, an HLX powered by accretion onto an intermediate-mass black hole (comparable to HLX-1) is unlikely to explain the observed variability and X-ray spectral shape of J0822+2241. We do also note that for a compact low-mass galaxy such as J0822+2241 an individual accreting intermediate-mass black hole as bright as $L_X \sim 10^{42}$ erg s$^{-1}$ would not be a "contaminant" with regard to the AGN scenario. However, a remaining question is whether or not a neutron-star-powered HLX could explain the observed properties of J0822+2241. The current brightest observed peak luminosity from a confirmed neutron star HLX is for NGC 5097 ULX 1, which is known to reach $L_X \sim 10^{41}$ erg s$^{-1}$ (F. Fürst et al. 2017; G. L. Israel et al. 2017), far lower than the luminosity found for J0822+2241. An interesting candidate HLX identified by D. J. Walton et al. (2022) and A. D. A. MacKenzie et al. (2023) could be associated with IC 1633, which corresponds to the only source in Figure 9 that is consistent with the epoch 2 luminosity measurement of J0822+2241 within the 2SXPS. However, as noted by A. D. A. MacKenzie et al. (2023), that source lies in a galaxy with strong diffuse X-ray emission that may contaminate the soft X-ray flux measurements by Swift and XMM-Newton. Regardless, if the current known neutron-star-powered HLX population is applicable to Green Pea galaxies, multiple sources would still be required to explain the X-ray spectral properties of J0822+2241. If, on the other hand, the X-ray flux from J0822+2241 were powered by the brightest neutron star HLX currently known, we reiterate that the source would need to reach 2–10 keV luminosities of $\gtrsim 10^{42}$ erg s$^{-1}$ on at least two separate occasions during a 6.2 yr baseline.

Our final consideration is thus whether a contribution of multiple U/HLXs within J0822+2241 could plausibly explain its observed X-ray properties. Such sources are known to exhibit a wide array of spectral variability (M. J. Middleton et al. 2015). Thus, at face value it seems possible that a population of unresolved (and causally disconnected) U/HLXs could produce a 2–10 keV luminosity exceeding $10^{42}$ erg s$^{-1}$ with a combined variability pattern resembling the observed hardening of the XMM-Newton spectrum of J0822+2241 from epoch 1 to epoch 2. A. D. Sutton et al. (2012) showed with high angular resolution Chandra observations that a seemingly bright off-nuclear X-ray source detected by XMM-Newton in the starburst galaxy NGC 2276 was in fact several unresolved ULXs. However, for the spectrum of J0822+2241 to be explained by ULXs alone would require $10 < N_{\mathrm{ULX}} < 1000$ individual sources with X-ray luminosities of $>10^{39}$ erg s$^{-1}$ $< L_X < 10^{41}$ erg s$^{-1}$ at the times of the epoch 1 and 2 XMM-Newton observations. Substantially higher numbers than this would also be needed if accounting for the expected transient nature of ULXs (e.g., M. Brightman et al. 2023). For the observed X-ray flux of J0822+2241 to be solely explained by HLXs, we would require $\lesssim$10 individual sources within the galaxy. Given that HLXs as a whole currently constitute ∼2%–4% of the entire detected ULX population (D. J. Walton et al. 2022; A. D. A. MacKenzie et al. 2023) >1 HLX in an individual galaxy is additionally unlikely.

Detailed studies of ULX populations in local galaxies have found a positive correlation between star formation rate and the number of ULXs detected, as well as a tentative enhanced star-formation-rate-normalized ULX rate at lower metallicities (e.g., M. Mapelli et al. 2010; D. A. Swartz et al. 2011). Considering the relation between star formation rate and ULX number from M. Mapelli et al. (2010), we would expect $\sim 20^{+50}_{-10}$ ULXs to be present in J0822+2241 if using the star formation rate of $37 \pm 4\,M_\odot\,\mathrm{yr}^{-1}$ calculated by C. Cardamone et al. (2009; with uncertainty quoted at the $1\sigma$ level), with a slight potential enhancement arising from its low metallicity. Such high numbers of ULXs in a single galaxy are extremely rare in the local Universe. One of the most extreme examples is that of the Cartwheel ring galaxy, with at least 29 ULXs associated (C. Salvaggio et al. 2023). However, conservatively including any off-nuclear sources studied by C. Salvaggio et al. (2023), the total average unabsorbed 0.5–10 keV luminosity from potential ULXs in the Cartwheel galaxy would be $L_{0.5-10\,\mathrm{keV}} \sim 2 \times 10^{41}$ erg s$^{-1}$ (C. Salvaggio et al.

2023), which is still a factor of five lower than the X-ray luminosity we find for J0822+2241. Furthermore, given existing ULX luminosity functions (e.g., W. Luangtip et al. 2015), the expected number of high-luminosity U/HLXs contained within a population of ∼20 U/HLXs would still be insufficient to explain the X-ray luminosity of J0822+2241.

A final test for the presence of U/HLXs in J0822+2241 that we consider is from radio observations. A. Borkar et al. (2024) presented Very Large Array 6 and 10 GHz observations of J0822+2241, finding an individual radio point source on ∼0.″6–1′ scales (∼3–5 kpc at the redshift of J0822+2241) coincident with the center of the galaxy. The general lack of off-center point sources and/or extension with the radio measurements already suggests that powerful off-nuclear contaminants are not present. Using the radio spectral index derived by A. Borkar et al. (2024), we find rest-frame 5 GHz/2–10 keV luminosity ratios of $\log R_X = -2.8 \pm 0.3$ and $-3.0 \pm 0.1$ for epochs 1 and 2, respectively. In comparison to the $\log R_X$ values measured by Y. Terashima & A. S. Wilson (2003), such values are entirely consistent with those expected from low-luminosity and Seyfert-like AGN. In addition, M. Mezcua et al. (2013, 2015) show that X-ray binaries are expected to have $\log R_X < -5.3$, in contrast to low-luminosity AGN with $-3.8 < \log R_X < -2.8$, the latter of which is consistent with J0822+2241 (see also M. Argo et al. 2018; A. Foord et al. 2025). Thus, the joint X-ray and radio properties of J0822+2241 show that its high X-ray luminosity can be accounted for without a dominant population of U/HLXs at radio or X-ray wavelengths.

Interestingly, A. Borkar et al. (2024) show that the radio fluxes detected for J0822+2241 are consistent with the expectations from numerous star formation rate relations in the literature if predicted from the star formation rate of C. Cardamone et al. (2009). However, this star formation rate was predicted with spectral fitting of the Hα line, for which our optical spectral fitting in Section 3.2 now suggests that an additional broad component is required. The presence of an AGN is known to often significantly bias estimates of star formation rate (e.g., K. Kouroumpatzakis et al. 2021, and references therein). For the case of J0822+2241, the broad component to Hα could indicate that the previous star formation rate is overestimated. We additionally note that our independent star formation rate measurement with `Lightning` in Section 3.3 is consistent with C. Cardamone et al. (2009), though with substantially wider uncertainties that reach $\sim 6\,M_\odot\,\mathrm{yr}^{-1}$ within 90% confidence. A lower star formation rate would yield a lower predicted star-formation-powered radio flux, which could then reveal an AGN-powered radio excess. The overall agreement between the radio-to-X-ray ratio of J0822+2241 and other radio-loud local AGN suggests a nonnegligible contribution to the radio emission from an AGN, which additionally supports the star formation rate of J0822+2241 being overestimated.

## 6. Relevance to JWST-detected AGN

R. Maiolino et al. (2025) recently presented a compilation of intermediate-to-high-redshift JWST-detected AGN with no detected X-ray counterparts in some of the deepest Chandra fields ever observed (see also T. T. Ananna et al. 2024; M. Yue et al. 2024). Though some of these undetected X-ray sources were the so-called elusive Little Red Dots (H. B. Akins et al. 2023; D. D. Kocevski et al. 2024), it is important to note that the X-ray nondetections are far more widespread than just this population, with almost every JWST-detected AGN in the compilation of R. Maiolino et al. (2025) lacking an X-ray counterpart. R. Maiolino et al. (2025) pose two possible solutions for the lack of X-ray detections: Compton-thick dust-free gas obscuration, or intrinsically soft X-ray spectra akin to narrow-line Seyfert 1 galaxies.

The broad Hα FWHM we find for J0822+2241 is fully consistent with the broad permitted line widths reported by M. Brooks et al. (2025) and R. Maiolino et al. (2025) for the type 1 JWST-detected AGN candidates displaying broad permitted lines. However, the equivalent width we measure is significantly below the median value found for the JWST AGN of 570 Å. The comparably low width constrained for the broad component of Hβ is consistent with some JWST broad Hα AGN candidates in which no significant broad Hβ component is detected (M. Brooks et al. 2025). However, our measured X-ray properties for J0822+2241 do not agree with either scenario posed by R. Maiolino et al. (2025) to explain the JWST AGN. We find minimal obscuration for J0822+2241 and a standard unobscured AGN intrinsic photon index of $\Gamma = 1.7^{+0.1}_{-0.2}$, far flatter than the steep shapes required to substantially deplete the observed X-ray flux from $z \gtrsim 6$ sources with Chandra, nor the typical photon indices of more local narrow-line Seyfert 1 AGN (e.g., C. Jin et al. 2012b). An obvious first question to ask then is, how does J0822+2241 compare to the JWST-detected AGN in terms of measured broad permitted Hα and X-ray constraints? Figure 10 plots the broad Hα luminosity versus 2–10 keV X-ray luminosity for the type 1 AGN in R. Maiolino et al. (2025), together with the measured values for J0822+2241 that are fully consistent with the vast majority of measured upper limits for JWST-detected type 1 AGN. We additionally include the broad Hα luminosity versus 2–10 keV luminosity relation of T. T. Shimizu et al. (2018) for type 1–1.2 AGN detected in the 70-month BAT catalog. The X-ray luminosity passband used in the relation was converted from 14–195 keV to 2–10 keV assuming a power law with a photon index of 1.8. To verify the X-ray passband conversion, we additionally show the narrow-component-subtracted Hα luminosity versus 2–10 keV luminosity relation found by C. Jin et al. (2012a) for type 1 and narrow-line Seyfert 1 AGN.

The overall disagreement of both the JWST AGN and J0822+2241 with the relations of T. T. Shimizu et al. (2018) and C. Jin et al. (2012a) is clearly striking. J0822+2241 lies ∼1–2 dex below the relations and is consistent with the (predominantly) X-ray-undetected JWST AGN. Given that J0822+2241 is one of the brightest Green Pea galaxies observed in X-rays (e.g., J. Svoboda et al. 2019; M. Singha et al. 2025), though comparable in terms of broad Hα luminosity (R. Lin et al. 2024; M. Singha et al. 2025), AGN within other Green Pea galaxies would likely lie at even lower X-ray fluxes. Our X-ray analysis of J0822+2241 offers a possibility that Green Pea galaxies are X-ray analogs of the broad-line JWST AGN candidates. However, comparing a single source to the predominantly undetected X-ray sample of R. Maiolino et al. (2025) is undoubtedly insufficient to draw conclusions on higher-redshift objects. We additionally note that, despite some similarities, the observed equivalent width of broad Hα we detect for J0822+2241 is below the values found by R. Maiolino et al. (2025), suggesting that the

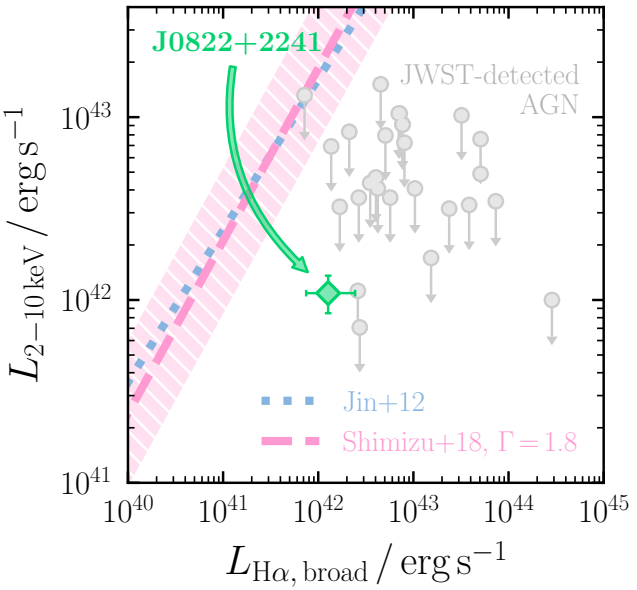


**Figure 10.** Comparison between broad H$\alpha$ luminosity and 2–10 keV luminosity measured for J0822+2241 and for the recent compilation of type 1 JWST-detected AGN from R. Maiolino et al. (2025). We additionally plot two relations between broad H$\alpha$ luminosity and X-ray luminosity derived from samples in the local Universe. First, we show with a pink dashed line (and associated shaded intrinsic scatter) the relation of T. T. Shimizu et al. (2018), constrained for type 1–1.2 AGN from the 70-month BAT catalog. The 2–10 keV luminosity for the relation was approximated from 14 to 195 keV by assuming a power law with photon index 1.8. For consistency, we additionally show the relation between narrow H$\alpha$-subtracted luminosity and 2–10 keV luminosity from C. Jin et al. (2012a) as a dotted blue line.

possibility of high covering factor Compton-thick broad-line region material in J0822+2241 is particularly unlikely.

If future detailed X-ray spectral analyses of more Green Pea galaxies find analogous properties to J0822+2241, as well as the JWST-detected broad-line AGN, alternative scenarios may be required to explain their X-ray deficit. For example, a possible explanation for apparent flux suppression in the X-ray and/or optical bands is for the observed light to be scattered emission from dense obscuration surrounding the AGN. A scattered component is often invoked in X-ray spectral fitting of obscured AGN to explain an excess of flux at ∼2–5 keV (e.g., C. Ricci et al. 2017a; P. G. Boorman et al. 2025). However, for a sufficiently Compton-thick AGN the scattered light component could dominate the entire X-ray spectral passband <10 keV (e.g., C. Greenwell et al. 2022; C. Greenwell et al. 2024). Away from X-rays, R. J. Assef et al. (2016, 2020) studied a subset of hot dust-obscured galaxies with unexpected blue ultraviolet-to-optical excesses, one of which was later confirmed to have a significant scattered component via imaging polarization (R. J. Assef et al. 2022). A significant scattered component could also potentially explain the broad H$\alpha$ emission detected in J0822+2241, although the intrinsic broad H$\alpha$ luminosity would have to be even higher than the current value, which could exacerbate the effect seen in Figure 10. The X-ray scattered fraction for Compton-thick AGN in the local Universe is expected to be $\lesssim$1% (K. K. Gupta et al. 2021) on average, such that the intrinsic X-ray luminosity of J0822+2241 would be $\gtrsim 10^{44}$ erg s$^{-1}$ if the observed XMM-Newton spectra were dominated by a scattered component. This is consistent with the findings of T. Kawamuro et al. (2019), who previously showed that a Compton-thick AGN with an intrinsic luminosity of $\log L_{2-10\,\mathrm{keV}}/\mathrm{erg\,s^{-1}} \gtrsim 43.8$ could self-consistently explain the near-to-mid-infrared properties of J0822+2241, as well as the nondetection from a 20 ks NuSTAR observation. Future polarimetric and/or higher-sensitivity hard X-ray observations (e.g., with a mission concept like HEX-P; K. K. Madsen et al. 2024) of J0822+2241 and other Green Pea galaxies could robustly search for evidence of significant scattered components arising from heavily obscured AGN.

## 7. Summary

We have presented the multiepoch X-ray spectral analysis of SDSS J082247.66+224144.0. Our key findings are as follows:

1. We find the observed 2–10 keV luminosity from two epochs separated by ∼6.2 yr to be entirely consistent, with observed rest-frame values of $\log L_{2-10\,\mathrm{keV}}/\mathrm{erg\,s^{-1}} = 42.0 \pm 0.3$ and $42.2 \pm 0.1$ for epochs 1 and 2, respectively (see Section 3). Such luminosities are seldom produced by sources other than an AGN, such that, based on luminosity arguments alone, we find J0822+2241 to be a strong AGN candidate.
2. We fit the archival SDSS optical spectrum of J0822+2241, finding a statistically significant requirement for a broad component to the H$\alpha$ line. We find an $\mathrm{FWHM}_{\mathrm{H}\alpha,\,\mathrm{broad}} = 1360^{+70}_{-100}$ km s$^{-1}$. Via fitting of the H$\beta$ line and the corresponding Balmer decrement derived from the ratio of narrow H$\alpha$ to H$\beta$, we derive an absorption-corrected broad H$\alpha$ luminosity of $\log L_{\mathrm{H}\alpha,\,\mathrm{broad,int}}/\mathrm{erg\,s^{-1}} = 42.1^{+0.3}_{-0.2}$. Assuming the predetermined black hole mass relation of A. E. Reines & M. Volonteri (2015), we estimate a broad H$\alpha$-based black hole mass of $M_{\mathrm{BH,H}\alpha} = 8^{+3}_{-2} \times 10^6\,M_\odot$ (see Sections 3.2 and 5.1).
3. To complement our X-ray and optical spectral analyses, we additionally collate and fit the broadband SED of J0822+2241 from X-ray to mid-infrared wavelengths with the `Lightning` code. We find that an AGN component is required to dominate at X-ray wavelengths, with a major contribution also expected in the near-infrared regime. Our fits additionally find that the AGN may provide a significant contribution in the UV-to-optical regime, though further analysis would be needed to confirm. Finally, we derive black hole and stellar masses from `Lightning` that are fully consistent with the relation of A. E. Reines & M. Volonteri (2015) (see Sections 3.3 and 4).
4. We show that the soft-band 0.5–2 keV flux of J0822+2241 has decreased significantly between the two epochs. If arising from a line-of-sight column density variation around an intrinsically nonvariable AGN, the column density would have increased by a factor of $\log(N_{\mathrm{H},2}/N_{\mathrm{H},1}) = 1.08^{+0.66}_{-0.72}$. Since the inclusion of a variable obscurer leads to an intrinsic photon index that is fully consistent with the Seyfert population and the general ubiquity of obscuration in AGN, we deem this scenario the most likely. Using a bolometric correction and the black hole mass constrained from our H$\alpha$ fitting, we estimate an Eddington ratio for J0822+2241 of $\lambda_{\mathrm{Edd}} = 1.4^{+0.4}_{-0.7}$%, potentially placing the source in (or close to) the unstable region of the effective Eddington limit on dusty gas (see Section 5.1).

5. We find the possibility of the soft X-ray flux variability having occurred from a single X-ray-unobscured AGN to be unlikely primarily based on the observed X-ray spectral shape changes between epochs 1 and 2. By considering a scenario in which the soft passband flux change was caused by a variable accretion disk component, we estimate that the black hole mass would need to be $1.1^{+36.0}_{-0.9} \times 10^4\,M_{\odot}$. However, given the super-Eddington accretion rates required to sustain the observed luminosity of J0822+2241, we deem our intermediate black hole mass estimate to be over-simplified and untrustworthy (see Section 5.2).
6. We investigate the possibility that the X-ray properties from J0822+2241 are the result of unresolved ULX and/or HLX sources in its host galaxy. If originating from a single off-nuclear source, J0822+2241 would be the highest-luminosity HLX ever discovered. We combine recently analyzed radio flux measurements of J0822+2241 to derive a 5 GHz/2–10 keV luminosity ratio that is additionally fully consistent with that expected from an AGN (see Section 5.3).
7. We compare the broad H$\alpha$ and X-ray luminosities of J0822+2241 to the values measured for a sample of JWST-detected type 1 AGN lacking detectable X-ray counterparts. We find the X-ray flux for J0822+2241 to be $\sim$1–2 dex lower than expected using relations derived from local populations of AGN. The observed X-ray deficit and/or broad H$\alpha$ luminosity excess is in agreement with the (predominantly undetected) X-ray fluxes found for JWST-detected broad-line AGN. However, our X-ray spectral analysis of J0822+2241 does not find obvious evidence for Compton-thick obscuration at $<$10 keV, nor intrinsically steep X-ray spectra, which were proposed previously to explain the X-ray deficit observed in JWST-detected AGN. We postulate that if future X-ray spectral analyses of Green Pea AGN and JWST-detected AGN show agreements, Green Pea galaxies may be useful for understanding black hole growth in compact galaxies in the early Universe (see Section 6).

Out of all the scenarios tested in this work, an AGN displaying obscuration variability is the only appropriate possibility to explain the X-ray properties of J0822+2241 observed by XMM-Newton. A fundamental requirement for this characterization is that the AGN dominates the observed X-ray spectrum at $<$10 keV. This is currently rare for the highly star-forming galaxy population, with non-AGN-related processes often concealing signatures of AGN activity $<$10 keV (e.g., B. D. Lehmer et al. 2023; M. Brightman et al. 2024; C. T. Richardson et al. 2025). Future high-sensitivity spectroscopy above 10 keV with capabilities like the High Energy X-ray Probe (HEX-P; K. K. Madsen et al. 2024) would be a powerful tool for correctly characterizing the census of AGN within low-mass, low-metallicity galaxies (including more extreme luminous compact galaxies) unveiled en masse by next-generation missions such as the UltraViolet Explorer (UVEX; S. R. Kulkarni et al. 2021). More broadly, given the current obstacles associated with detecting high-redshift JWST-detected AGN candidates in X-rays (e.g., T. T. Ananna et al. 2024; M. Yue et al. 2024; R. Maiolino et al. 2025), our work shows that future dedicated X-ray campaigns of local analogs may prove fruitful for a complete understanding of black hole growth at high redshift.

## Acknowledgments

We thank the anonymous reviewer for their useful comments that helped to improve the manuscript. P.G.B. acknowledges support under NASA grant 80NSSC25K7089 and NASA contract NNG08FD60C. P.G.B., J.S., A.B., and K. K. also acknowledge financial support from the Czech Science Foundation under project No. 22-22643S. B.A. acknowledges financial support from Charles University under GAUK project No. 345625. The work of D.S. was carried out at the Jet Propulsion Laboratory, California Institute of Technology, under a contract with NASA. R.J.A. was supported by FONDECYT grant No. 1231718 and by the ANID BASAL project FB210003. D.J.W. acknowledges support from the Science and Technology Facilities Council (STFC; grant code ST/Y001060/1).

This research has made use of the NASA/IPAC Extragalactic Database (NED), which is operated by the Jet Propulsion Laboratory, California Institute of Technology, under contract with the National Aeronautics and Space Administration.

This research has made use of NASA's Astrophysics Data System Bibliographic Services.

*Facility:* `XMM-Newton`.

*Software:* This paper made extensive use of `matplotlib` (J. D. Hunter 2007), `pandas` (The pandas development team 2020; W. McKinney 2010) and `astropy` (Astropy Collaboration et al. 2013, 2018, 2022).

## Appendix
## Updated Palomar Spectroscopy

As a means to investigate the temporal properties of the optical spectrum of J0822+2241, we acquired follow-up spectroscopy with the Palomar/DoubleSpec spectrograph on UT 2024 October 4. Given that the SDSS spectrum was taken in 2004, our follow-up Palomar spectroscopy covers an observed baseline of $\sim$20 yr or $\sim$16 yr in the rest-frame of J0822+2241. We apply an additional linear correction to wavelength and flux of the Palomar spectrum in order to match the observed narrow lines in the spectrum. We find an acceptable match in the [O II] $\lambda\lambda$4959, 5507 and [S II] $\lambda\lambda$6716, 6731 narrow lines by shifting the spectrum 2.1 Å redward and increasing the observed flux by a multiplicative factor of 2.1. The original SDSS and correct Palomar spectra are overplotted in Figure A1. There are no obvious changes in any key line profiles, in particular for the H$\alpha$ $\lambda$6563 + [N II] $\lambda\lambda$6548, 6583. The consistency over an $\sim$16 yr baseline strongly suggests that the broad component to H$\alpha$ that we detect cannot arise from a single supernova, for which the broad component would be expected to decay on the order of years (e.g., Y. I. Izotov et al. 2007; C. Simmonds et al 2016).

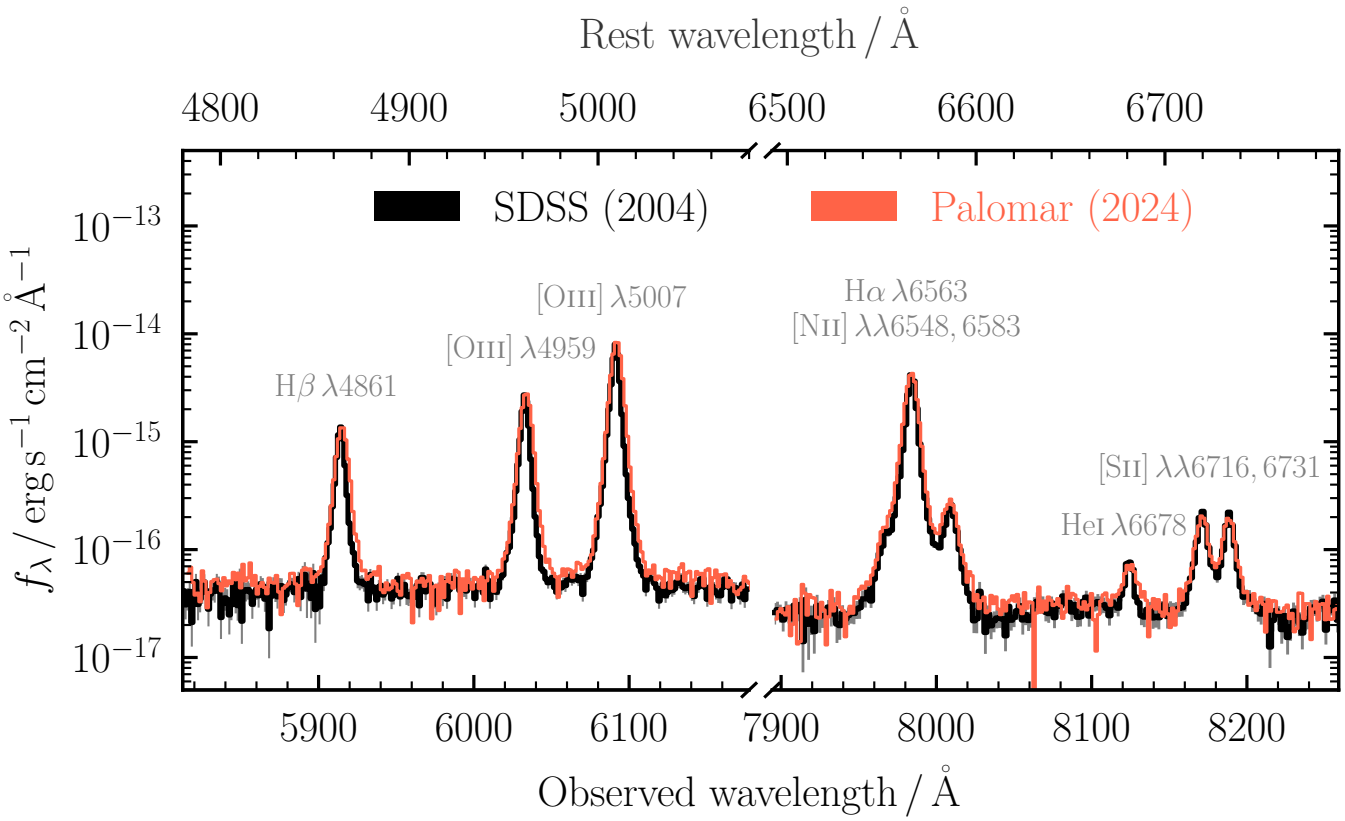


**Figure A1.** Comparison between the line profiles measured by SDSS and Palomar/DoubleSpec, shown with thick black and thinner red lines, respectively. From left to right, we show H$\beta$ $\lambda$4861, [O II] $\lambda\lambda$4959, 5507, H$\alpha$ $\lambda$6563, [N II] $\lambda\lambda$6548, 6583, HeI $\lambda$6678, and [S II] $\lambda\lambda$6716, 6731. After applying a simple translation in wavelength and flux, the observed spectra are considerably similar, shifted by comparable amounts in relative flux and absolute wavelength. Even without applying a translation to the Palomar spectrum, all line profiles are qualitatively similar, suggesting a lack of spectral variability for the H$\alpha$ line profile over an $\sim$16 yr rest-frame baseline.

## ORCID iDs

Peter G. Boorman https://orcid.org/0000-0001-9379-4716
Jiří Svoboda https://orcid.org/0000-0003-2931-0742
Daniel Stern https://orcid.org/0000-0003-2686-9241
Bret D. Lehmer https://orcid.org/0000-0003-2192-3296
Abhijeet Borkar https://orcid.org/0000-0002-9807-4520
Murray Brightman https://orcid.org/0000-0002-8147-2602
Hannah P. Earnshaw https://orcid.org/0000-0001-5857-5622
Fiona A. Harrison https://orcid.org/0000-0002-4226-8959
Konstantinos Kouroumpatzakis https://orcid.org/0000-0002-1444-2016
Barbora Adamcová https://orcid.org/0009-0008-6899-4749
Roberto J. Assef https://orcid.org/0000-0002-9508-3667
Matthias Ehle https://orcid.org/0000-0002-2171-2926
Brian Grefenstette https://orcid.org/0000-0002-1984-2932
Romana Grossová https://orcid.org/0000-0003-3471-7459
Maitrayee Gupta https://orcid.org/0000-0003-0976-8932
Elias Kammoun https://orcid.org/0000-0002-0273-218X
Taiki Kawamuro https://orcid.org/0000-0002-6808-2052
Lea Marcotulli https://orcid.org/0000-0002-8472-3649
Romana Mikušincová https://orcid.org/0000-0001-7374-843X
Matthew J. Middleton https://orcid.org/0000-0002-8183-2970
Edward Nathan https://orcid.org/0000-0002-9633-9193
Joanna M. Piotrowska https://orcid.org/0000-0003-1661-2338
Jean J. Somalwar https://orcid.org/0000-0001-8426-5732
Núria Torres-Albà https://orcid.org/0000-0003-3638-8943
Dominic J. Walton https://orcid.org/0000-0001-5819-3552
Daniel R. Weisz https://orcid.org/0000-0002-6442-6030

## References

Adamcová, B., Svoboda, J., Kyritsis, E., et al. 2024, A&A, 691, A27
Aird, J., Coil, A. L., Georgakakis, A., et al. 2015, MNRAS, 451, 1892
Akins, H. B., Casey, C. M., Allen, N., et al. 2023, ApJ, 956, 61
Ananna, T. T., Bogdán, Á., Kovács, O. E., Natarajan, P., & Hickox, R. C. 2024, ApJL, 969, L18
Ananna, T. T., Urry, C. M., Ricci, C., et al. 2022, ApJL, 939, L13
Annuar, A., Alexander, D. M., Gandhi, P., et al. 2020, MNRAS, 497, 229
Argo, M., Coppola, J., Mezcua, M., Earnshaw, H., & Roberts, T. 2018, in 14th European VLBI Network Symp. and Users Meeting (EVN 2018), ed. I. Agudo, A. Alberdi, J. E. Conway, & M. Lindqvist (Trieste: SISSA), 23
Arnaud, K. A. 1996, in ASP Conf. Ser. 101, Astronomical Data Analysis Software and Systems V, ed. G. H. Jacoby & J. Barnes (San Francisco, CA: ASP), 17
Asmus, D., Greenwell, C. L., Gandhi, P., et al. 2020, MNRAS, 494, 1784
Assef, R. J., Bauer, F. E., Blain, A. W., et al. 2022, ApJ, 934, 101
Assef, R. J., Brightman, M., Walton, D. J., et al. 2020, ApJ, 897, 112
Assef, R. J., Stern, D., Noirot, G., et al. 2018, ApJS, 234, 23
Assef, R. J., Walton, D. J., Brightman, M., et al. 2016, ApJ, 819, 111
Asthana, S., Haehnelt, M. G., Kulkarni, G., et al. 2024, arXiv:2409.15453
Astropy Collaboration, Price-Whelan, A. M., Lim, P. L., et al. 2022, ApJ, 935, 167
Astropy Collaboration, Price-Whelan, A. M., Sipőcz, B. M., et al. 2018, AJ, 156, 123
Astropy Collaboration, Robitaille, T. P., Tollerud, E. J., et al. 2013, A&A, 558, A33
Baldwin, J. A., Phillips, M. M., & Terlevich, R. 1981, PASP, 93, 5

Baronchelli, L., Nandra, K., & Buchner, J. 2020, MNRAS, 498, 5284
Boorman, P. G., Gandhi, P., Buchner, J., et al. 2025, ApJ, 978, 118
Boorman, P. G., Stern, D., Assef, R. J., et al. 2024a, ApJ, 975, 230
Boorman, P. G., Torres-Albà, N., Annuar, A., et al. 2024b, FrASS, 11, 1335459
Borkar, A., Grossová, R., Svoboda, J., et al. 2024, A&A, 687, A137
Bouwens, R. J., Illingworth, G. D., Oesch, P. A., et al. 2015, ApJ, 811, 140
Brandt, W. N., & Alexander, D. M. 2015, A&ARv, 23, 1
Brightman, M., Hameury, J.-M., Lasota, J.-P., et al. 2023, ApJ, 951, 51
Brightman, M., Margutti, R., Polzin, A., et al. 2024, FrASS, 10, 1292656
Brinchmann, J., Charlot, S., White, S. D. M., et al. 2004, MNRAS, 351, 1151
Brooks, M., Simons, R. C., Trump, J. R., et al. 2025, ApJ, 986, 177
Brorby, M., Kaaret, P., Prestwich, A., & Mirabel, I. F. 2016, MNRAS, 457, 4081
Buchner, J., 2016 BXA: Bayesian X-ray Analysis, Astrophysics Source Code Library, ascl:1610.011
Buchner, J. 2021, JOSS, 6, 3001
Buchner, J., & Boorman, P. 2023, Statistical Aspects of X-ray Spectral Analysis (Singapore: Springer)
Buchner, J., Georgakakis, A., Nandra, K., et al. 2014, A&A, 564, A125
Buchner, J., Georgakakis, A., Nandra, K., et al. 2015, ApJ, 802, 89
Buchner, J., Starck, H., Salvato, M., et al. 2024, A&A, 692, A161
Calzetti, D., Armus, L., Bohlin, R. C., et al. 2000, ApJ, 533, 682
Cappellari, M., & Emsellem, E. 2004, PASP, 116, 138
Cardamone, C., Schawinski, K., Sarzi, M., et al. 2009, MNRAS, 399, 1191
Cash, W. 1979, ApJ, 228, 939
Civano, F., Zhao, X., Boorman, P. G., et al. 2024, FrASS, 11, 1340719
Crummy, J., Fabian, A. C., Gallo, L., & Ross, R. R. 2006, MNRAS, 365, 1067
Domínguez, A., Siana, B., Henry, A. L., et al. 2013, ApJ, 763, 145
Done, C., Davis, S. W., Jin, C., Blaes, O., & Ward, M. 2012, MNRAS, 420, 1848
Dong, X.-B., Ho, L. C., Yuan, W., et al. 2012, ApJ, 755, 167
Doore, K., Monson, E. B., Eufrasio, R. T., et al. 2023, ApJS, 266, 39
Dovčiak, M., Karas, V., & Yaqoob, T. 2004, ApJS, 153, 205
Dovčiak, M., Muleri, F., Goosmann, R. W., Karas, V., & Matt, G. 2008, MNRAS, 391, 32
Duras, F., Bongiorno, A., Ricci, F., et al. 2020, A&A, 636, A73
Dwarkadas, V. V. 2014, MNRAS, 440, 1917
Dwarkadas, V. V., & Gruszko, J. 2012, MNRAS, 419, 1515
Evans, I. N., Primini, F. A., Miller, J. B., et al. 2020, AAS Meeting, 235, 154.05
Evans, P. A., Page, K. L., Osborne, J. P., et al. 2020, ApJS, 247, 54
Fabian, A. C., Vasudevan, R. V., & Gandhi, P. 2008, MNRAS, 385, L43
Feroz, F., Hobson, M. P., & Bridges, M. 2009, MNRAS, 398, 1601
Filippenko, A. V., & Sargent, W. L. W. 1988, ApJ, 324, 134
Filippenko, A. V., & Sargent, W. L. W. 1989, ApJL, 342, L11
Fitzpatrick, E. L. 1999, PASP, 111, 63
Fontanot, F., Cristiani, S., & Vanzella, E. 2012, MNRAS, 425, 1413
Foord, A., Civano, F., Comerford, J. M., et al. 2025, ApJ, 984, 79
Fragos, T., Lehmer, B. D., Naoz, S., Zezas, A., & Basu-Zych, A. 2013, ApJL, 776, L31
Franeck, A., Wünsch, R., Martìnez-González, S., et al. 2022, ApJ, 927, 212
Fürst, F., Walton, D. J., Stern, D., et al. 2017, ApJ, 834, 77
Gabriel, C., Denby, M., Fyfe, D. J., et al. 2004, in ASP Conf. Ser. 314, Astronomical Data Analysis Software and Systems (ADASS) XIII, ed. F. Ochsenbein, M. G. Allen, & D. Egret (San Francisco, CA: ASP), 759
Gao, Y., Wang, Q. D., Appleton, P. N., & Lucas, R. A. 2003, ApJL, 596, L171
Gardner, J. P., Mather, J. C., Abbott, R., et al. 2023, PASP, 135, 068001
Gierliński, M., & Done, C. 2004, MNRAS, 349, L7
Gordon, C., & Arnaud, K., 2021 PyXspec: Python Interface to XSPEC Spectral-fitting Program, Astrophysics Source Code Library, ascl:2101.014
Greene, J. E., & Ho, L. C. 2004, ApJ, 610, 722
Greene, J. E., Labbe, I., Goulding, A. D., et al. 2024, ApJ, 964, 39
Greenwell, C., Gandhi, P., Lansbury, G., et al. 2022, ApJL, 934, L34
Greenwell, C., Gandhi, P., Stern, D., et al. 2024, MNRAS, 527, 12065
Gupta, K. K., Ricci, C., Tortosa, A., et al. 2021, MNRAS, 504, 428
Gutiérrez, C. P., Anderson, J. P., Hamuy, M., et al. 2017, ApJ, 850, 89
Haardt, F., & Salvaterra, R. 2015, A&A, 575, L16
Hainline, K. N., Reines, A. E., Greene, J. E., & Stern, D. 2016, ApJ, 832, 119
Harikane, Y., Zhang, Y., Nakajima, K., et al. 2023, ApJ, 959, 39
Harrison, F. A., Craig, W. W., Christensen, F. E., et al. 2013, ApJ, 770, 103
Hickox, R. C., & Alexander, D. M. 2018, ARA&A, 56, 625
Ho, L. C., Filippenko, A. V., Sargent, W. L. W., & Peng, C. Y. 1997, ApJS, 112, 391
Hunter, J. D. 2007, CSE, 9, 90
Israel, G. L., Belfiore, A., Stella, L., et al. 2017, Sci, 355, 817
Izotov, Y. I., Guseva, N. G., & Thuan, T. X. 2011, ApJ, 728, 161
Izotov, Y. I., Orlitová, I., Schaerer, D., et al. 2016, Natur, 529, 178
Izotov, Y. I., Thuan, T. X., & Guseva, N. G. 2007, ApJ, 671, 1297
Jansen, F., Lumb, D., Altieri, B., et al. 2001, A&A, 365, L1
Jarrett, T. H., Cohen, M., Masci, F., et al. 2011, ApJ, 735, 112
Jin, C., Ward, M., & Done, C. 2012a, MNRAS, 422, 3268
Jin, C., Ward, M., Done, C., & Gelbord, J. 2012b, MNRAS, 420, 1825
Juodžbalis, I., Maiolino, R., Baker, W. M., et al. 2025, arXiv:2504.03551
Kara, E., & García, J. 2025, arXiv:2503.22791
Kauffmann, G., Heckman, T. M., White, S. D. M., et al. 2003, MNRAS, 341, 33
Kawamuro, T., Ueda, Y., Ichikawa, K., et al. 2019, ApJ, 881, 48
King, A., Lasota, J.-P., & Middleton, M. 2023, NewAR, 96, 101672
Kocevski, D. D., Onoue, M., Inayoshi, K., et al. 2023, ApJL, 954, L4
Kocevski, D. D., Finkelstein, S. L., Barro, G., et al. 2024, ApJ, 986, 126
Kouroumpatzakis, K., Svoboda, J., Zezas, A., et al. 2024, A&A, 688, A159
Kouroumpatzakis, K., Zezas, A., Maragkoudakis, A., et al. 2021, MNRAS, 506, 3079
Kubota, A., & Done, C. 2018, MNRAS, 480, 1247
Kulkarni, S. R., Harrison, F. A., Grefenstette, B. W., et al. 2021, arXiv:2111.15608
Kyritsis, E., Zezas, A., Haberl, F., et al. 2025, A&A, 694, A128
Lefkir, M., Kammoun, E., Barret, D., et al. 2023, MNRAS, 522, 1169
Lehmer, B. D., Alexander, D. M., Bauer, F. E., et al. 2010, ApJ, 724, 559
Lehmer, B. D., Eufrasio, R. T., Basu-Zych, A., et al. 2021, ApJ, 907, 17
Lehmer, B. D., Garofali, K., Binder, B. A., et al. 2023, FrASS, 10, 1293918
Lehmer, B. D., Monson, E. B., Eufrasio, R. T., et al. 2024, ApJ, 977, 189
Lin, R., Zheng, Z.-Y., Jiang, C., et al. 2025, ApJL, 980, L34
Lin, R., Zheng, Z.-Y., Yuan, F.-T., et al. 2024, SCPMA, 67, 109811
Liu, W.-J., Ho, L. C., Dong, X.-B., Yao, S., & Lira, P. 2025, arXiv:2503.12898
Loeb, A., & Barkana, R. 2001, ARA&A, 39, 19
Luangtip, W., Roberts, T. P., Mineo, S., et al. 2015, MNRAS, 446, 470
MacKenzie, A. D. A., Roberts, T. P., & Walton, D. J. 2023, AN, 344, e20230028
Madathil-Pottayil, A., Walton, D. J., Garcìa, J., et al. 2024, MNRAS, 534, 608
Madau, P., Giallongo, E., Grazian, A., & Haardt, F. 2024, ApJ, 971, 75
Madsen, K. K., Garcìa, J. A., Stern, D., et al. 2024, FrASS, 11, 1357834
Maiolino, R., Risaliti, G., Signorini, M., et al. 2025, MNRAS, 538, 1921
Mapelli, M., Ripamonti, E., Zampieri, L., Colpi, M., & Bressan, A. 2010, MNRAS, 408, 234
Markowitz, A. G., Krumpe, M., & Nikutta, R. 2014, MNRAS, 439, 1403
Martins, F., Schaerer, D., Haemmerlé, L., & Charbonnel, C. 2020, A&A, 633, A9
Mateos, S., Alonso-Herrero, A., Carrera, F. J., et al. 2012, MNRAS, 426, 3271
Matthee, J., Mackenzie, R., Simcoe, R. A., et al. 2023, ApJ, 950, 67
McKinney, W. 2010, in Proc. of the 9th Python in Science Conf., ed. S. van der Walt & J. Millman, 56
Mezcua, M., Lobanov, A. P., & Martí-Vidal, I. 2013, MNRAS, 436, 2454
Mezcua, M., Roberts, T. P., Lobanov, A. P., & Sutton, A. D. 2015, MNRAS, 448, 1893
Middleton, M. J., Heil, L., Pintore, F., Walton, D. J., & Roberts, T. P. 2015, MNRAS, 447, 3243
Monson, E. B., Doore, K., Eufrasio, R. T., et al. 2023, ApJ, 951, 15
Naidu, R. P., Oesch, P. A., van Dokkum, P., et al. 2022, ApJL, 940, L14
Nandra, K., & Pounds, K. A. 1994, MNRAS, 268, 405
Osterbrock, D. E. 1989, Astrophysics of Gaseous Nebulae and Active Galactic Nuclei (Mill Valley, CA: Univ. Science Books)
Page, M. J., Brindle, C., Talavera, A., et al. 2012, MNRAS, 426, 903
Pizzetti, A., Torres-Albà, N., Marchesi, S., et al. 2025, ApJ, 979, 170
Reefe, M., Sexton, R. O., Doan, S. M., et al. 2023, ApJS, 265, 21
Reines, A. E., Greene, J. E., & Geha, M. 2013, ApJ, 775, 116
Reines, A. E., & Volonteri, M. 2015, ApJ, 813, 82
Ricci, C., Ananna, T. T., Temple, M. J., et al. 2022, ApJ, 938, 67
Ricci, C., Ichikawa, K., Stalevski, M., et al. 2023, ApJ, 959, 27
Ricci, C., Trakhtenbrot, B., Koss, M. J., et al. 2017a, ApJS, 233, 17
Ricci, C., Trakhtenbrot, B., Koss, M. J., et al. 2017b, Natur, 549, 488
Ricci, C., Ueda, Y., Koss, M. J., et al. 2015, ApJL, 815, L13
Richardson, C. T., Wels, J., Garofali, K., et al. 2025, arXiv:250507749R
Risaliti, G., Elvis, M., & Nicastro, F. 2002, ApJ, 571, 234
Rivers, E., Markowitz, A., & Rothschild, R. 2011, ApJL, 742, L29
Robertson, B. E., Ellis, R. S., Furlanetto, S. R., & Dunlop, J. S. 2015, ApJL, 802, L19
Salvaggio, C., Wolter, A., Belfiore, A., & Colpi, M. 2023, MNRAS, 522, 1377
Satyapal, S., Abel, N. P., & Secrest, N. J. 2018, ApJ, 858, 38
Schlafly, E. F., & Finkbeiner, D. P. 2011, ApJ, 737, 103

Servillat, M., Farrell, S. A., Lin, D., et al. 2011, ApJ, 743, 6
Shapiro, P. R., & Giroux, M. L. 1987, ApJL, 321, L107
Shimizu, T. T., Davies, R. I., Koss, M., et al. 2018, ApJ, 856, 154
Simmonds, C., Bauer, F. E., Thuan, T. X., et al. 2016, A&A, 596, A64
Singha, M., Sarmiento, J., Malhotra, S., et al. 2025, ApJ, 984, 155
Smith, M. J. S. 2025, XMM-SOC-CAL -TN-0018, EPIC Consortium
Stalevski, M., Fritz, J., Baes, M., Nakos, T., & Popović, L. Č. 2012, MNRAS, 420, 2756
Stalevski, M., Ricci, C., Ueda, Y., et al. 2016, MNRAS, 458, 2288
Stern, D., Assef, R. J., Benford, D. J., et al. 2012, ApJ, 753, 30
Strüder, L., Briel, U., Dennerl, K., et al. 2001, A&A, 365, L18
Sturm, M. R., Hayes, B., & Reines, A. E. 2025, ApJ, 979, 36
Sutton, A. D., Roberts, T. P., Walton, D. J., Gladstone, J. C., & Scott, A. E. 2012, MNRAS, 423, 1154
Svoboda, J., Douna, V., Orlitová, I., & Ehle, M. 2019, ApJ, 880, 144
Swartz, D. A., Soria, R., Tennant, A. F., & Yukita, M. 2011, ApJ, 741, 49
Tanimoto, A., Ueda, Y., Odaka, H., Yamada, S., & Ricci, C. 2022, ApJS, 260, 30
Terashima, Y., & Wilson, A. S. 2003, ApJ, 583, 145
The pandas development team 2020, pandas-dev/pandas: Pandas v1.5.3, doi:10.5281/zenodo.3509134
Torres-Albà, N., Bosch-Ramon, V., & Iwasawa, K. 2020, A&A, 635, A57
Torres-Albà, N., Marchesi, S., Zhao, X., et al. 2021, ApJ, 922, 252
Torres-Albà, N., Marchesi, S., Zhao, X., et al. 2023, A&A, 678, A154
Turner, M. J. L., Abbey, A., Arnaud, M., et al. 2001, A&A, 365, L27
Übler, H., Maiolino, R., Pérez-González, P. G., et al. 2024, MNRAS, 531, 355
Ueda, Y., Akiyama, M., Hasinger, G., Miyaji, T., & Watson, M. G. 2014, ApJ, 786, 104
Vianello, G. 2018, ApJS, 236, 17
Wachter, K., Leach, R., & Kellogg, E. 1979, ApJ, 230, 274
Waddell, S. G. H., Nandra, K., Buchner, J., et al. 2024, A&A, 690, A132
Walton, D. J., Mackenzie, A. D. A., Gully, H., et al. 2022, MNRAS, 509, 1587
Walton, D. J., Risaliti, G., Harrison, F. A., et al. 2014, ApJ, 788, 76
Walton, D. J., Zoghbi, A., Cackett, E. M., et al. 2013, ApJL, 777, L23
Webb, N. A., Coriat, M., Traulsen, I., et al. 2020, A&A, 641, A136
Willingale, R., Starling, R. L. C., Beardmore, A. P., Tanvir, N. R., & O'Brien, P. T. 2013, MNRAS, 431, 394
Wilms, J., Allen, A., & McCray, R. 2000, ApJ, 542, 914
Yang, G., Caputi, K. I., Papovich, C., et al. 2023, ApJL, 950, L5
Yang, H., Malhotra, S., Gronke, M., et al. 2017, ApJ, 844, 171
York, D. G., Adelman, J., Anderson, J. E. J., et al. 2000, AJ, 120, 1579
Yue, M., Eilers, A.-C., Ananna, T. T., et al. 2024, ApJL, 974, L26